Oligodendroglial macroautophagy is essential for myelin sheath turnover to prevent neurodegeneration and death

Etan R. Aber[1,2,9], **Christopher J. Griffey**[1,2,9], **Tim Davies**[3,4], **Alice M. Li**[5,6,8], **Young Joo Yang**[7], **Katherine R. Croce**[2,7], **James E. Goldman**[3], **Jaime Grutzendler**[5], **Julie C. Canman**[3], **Ai Yamamoto**[2,3,10,*]

[1]Doctoral Program in Neurobiology and Behavior, Medical Scientist Training Program, Columbia University, New York, NY 10032, USA

[2]Department of Neurology, Columbia University, New York, NY 10032, USA

[3]Department of Pathology and Cell Biology, Columbia University, New York, NY 10032, USA

[4]Department of Biosciences, Durham University, Durham DH1 3LE, UK

[5]Department of Neurology and Neuroscience, Yale University, New Haven, CT 06515, USA

[6]Interdepartmental Neuroscience Program, Yale School of Medicine, New Haven, CT 06510, USA

[7]Graduate Program in Pathobiology and Molecular Medicine, Columbia University, New York, NY 10032, USA

[8]Present address: Department of Pathology, Brigham and Women's Hospital and Harvard Medical School, Boston, MA 02115, USA

[9]These authors contributed equally

[10]Lead contact

SUMMARY

Although macroautophagy deficits are implicated across adult-onset neurodegenerative diseases, we understand little about how the discrete, highly evolved cell types of the central nervous system use macroautophagy to maintain homeostasis. One such cell type is the oligodendrocyte, whose myelin sheaths are central for the reliable conduction of action potentials. Using an integrated

approach of mouse genetics, live cell imaging, electron microscopy, and biochemistry, we show that mature oligodendrocytes require macroautophagy to degrade cell autonomously their myelin by consolidating cytosolic and transmembrane myelin proteins into an amphisome intermediate prior to degradation. We find that disruption of autophagic myelin turnover leads to changes in myelin sheath structure, ultimately impairing neural function and culminating in an adult-onset progressive motor decline, neurodegeneration, and death. Our model indicates that the continuous and cell-autonomous maintenance of the myelin sheath through macroautophagy is essential, shedding insight into how macroautophagy dysregulation might contribute to neurodegenerative disease pathophysiology.

Graphical Abstract
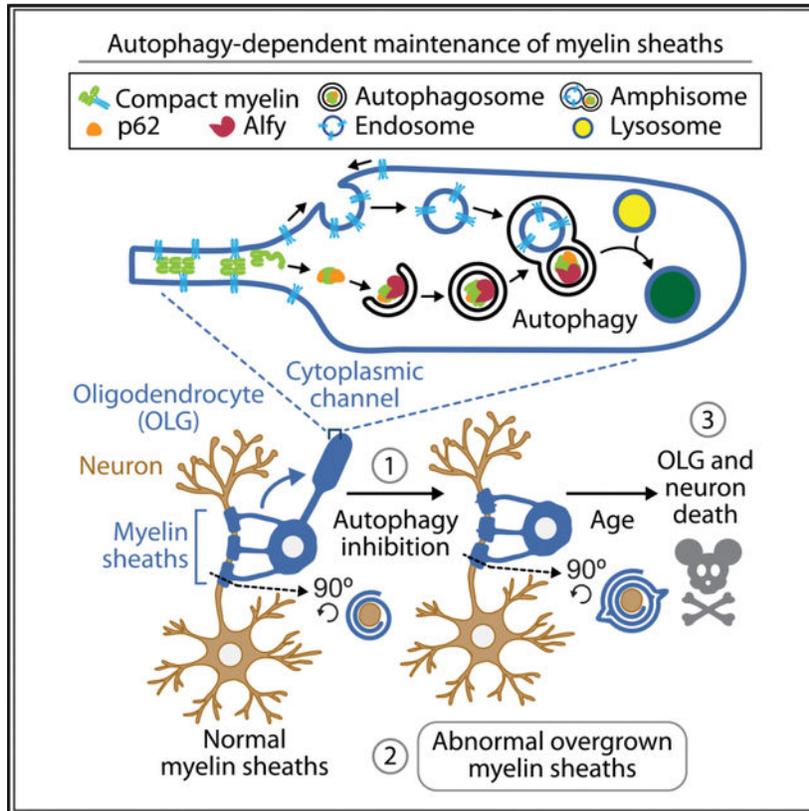
In brief

Oligodendrocytes assemble myelin and support the axons they myelinate. Aber et al. report that oligodendrocytes coordinate autophagy and endocytosis to turn over myelin. The absence of oligodendroglial autophagy causes myelin abnormalities, behavioral dysfunction, glial and neurodegeneration, and death, demonstrating the importance of this process for a healthy CNS.

INTRODUCTION

Oligodendroglial myelin sheaths facilitate the proper conduction of action potentials, a fundamental facet to central nervous system (CNS) function. Defects in myelination are

catastrophic in vertebrates and contribute to the neuropathology of diseases ranging from multiple sclerosis to Alzheimer disease (Franklin and Ffrench-Constant, 2017). Despite its importance, little is known about how myelination is maintained in the aging organism.

Although long-considered static elements in the adult CNS (Kondiles and Horner, 2017), recent studies have shown oligodendrocytes (OLGs), myelination, and white matter architecture changes in the adult brain in response to circuit alterations, suggesting that myelination is adaptable throughout life. In mice, the formation of new OLGs appears to be a major contributor to these changes (reviewed in Williamson and Lyons [2018]). In humans, the vast majority of OLGs are long lived and persist throughout life, and the myelin proteins turn over continuously with a half-life of months (Yeung et al., 2014). Studies also indicate that mature OLGs do not generate myelin sheaths *de novo* (Crang et al., 1998; Crawford et al., 2016; Czopka et al., 2013; Jeffries et al., 2016; Keirstead and Blakemore, 1997; Makinodan et al., 2013; Watkins et al., 2008), suggesting that OLG turnover alone may not fully explain myelin maintenance. To achieve myelin dynamicity, we hypothesize that cell-autonomous myelin turnover plays a critical role in modulating and maintaining neural circuits.

Myelin is a specialized adaptation of the cholesterol- and sphingolipid-enriched oligodendroglial plasma membrane, where much of the upper and lower plasma membranes are held tightly together by oligomers of myelin basic protein (MBP) (Aggarwal et al., 2011b) to keep the space between the membranes devoid of most cytosol and organelles. These thin sheaths, edged with cytoplasmic channels, enwrap the axon by displacing previously deposited membrane layers against the axon (Djannatian et al., 2019; Snaidero et al., 2014). Although remarkably long lived, the myelin sheath needs to be renewed and is believed to be dynamic (Fischer and Morell, 1974; Hill et al., 2018; Savas et al., 2012; Wang et al., 2020). Despite many insights into myelin synthesis (Aggarwal et al., 2011a; Emery et al., 2009; Snaidero et al., 2017), the mechanism underlying myelin degradation is unknown. We postulated that the complex structure of myelin—with its unique cytosolic and membrane components—would require the coordination of autophagy and endocytosis for its degradation.

We report that OLGs not only use macroautophagy to turnover their myelin but also find that it is essential for maintaining functional neuronal circuitry and CNS health. Although genetic inactivation of oligodendroglial macroautophagy in mice led to no detectable defects in myelination for up to 2 months of age, mice later demonstrated an age-dependent increase in myelin thickness and in appearance of abnormal myelin structures, accompanied by behavioral abnormalities, neurodegeneration, and premature lethality. In addition, live imaging of mature OLGs *in vitro* reveals that autophagosome biogenesis and acidification occur throughout the cell, including within the sheath's cytoplasmic channels, and that through the formation of amphisome intermediates, autophagy degrades both cytosolic and membranous components of the myelin sheath.

RESULTS

Macroautophagy is required to continuously remodel the myelin sheaths of the adult CNS

To examine the role macroautophagy plays in myelin sheath maintenance, we used a Cre recombinase expressed through the *CNP1* locus (CNP[Cre]) (Lappe-Siefke et al., 2003) to conditionally inactivate macroautophagy in OLGs via homozygous deletion of *Atg7* (Atg7cKO) (Komatsu et al., 2005). As expected, the autophagy adaptor protein p62 accumulated in Atg7cKO but not in heterozygous (Atg7cHet) or *Atg7[loxP/loxP]* (Atg7^{fl/fl}) white matter (Figures S1A and S1B). Despite the complete inactivation of macroautophagy, we observed no demonstrable difference in the viability or behavior of Atg7cKO mice out to 2 months old (Figures S1C–S1G; Video S1). Transcription of myelin proteins was unaffected (Figure S1H), and analyses of forebrain white matter indicated that the numbers of OLG progenitor cells (OPCs) and mature OLGs were also similar across genotype (Figures S1I and S1J). These data suggest that the CNP[Cre]-mediated genetic inactivation of macroautophagy in the oligodendroglial lineage in Atg7cKO mice did not affect oligodendrogliogenesis or biogenesis of the myelin sheath. Similar results were obtained upon conditional deletion of *Atg5*, which is also required for autophagosome formation (Hara et al., 2006; Komatsu et al., 2006) (data not shown).

We next performed ultrastructural studies in the adult CNS white matter (Figure 1). Although myelin sheath thickness was similar across genotypes at 2 months old, it increased in Atg7cKO mice with age (Figures 1A–1H). Myelin periodicity, however, was unaffected (Figure S1K, L). Analyses of g-ratio per axon diameter in the optic nerve indicated that the g-ratios in Atg7cKO mice were significantly smaller, with only the thickest axons showing no significant difference (Figures 1A–1F). The corpus callosum revealed similarly dramatic differences in sheath thickness (Figures 1G and 1H), and both brain regions also demonstrated an increased prevalence of abnormal myelin structures (Figures 1I and S1M). Although a previous report suggested no difference at younger ages (Saraswat Ohri et al., 2018), myelination in 16-month-old spinal cords was affected in Atg7cKO mice (Figures S1N–S1P), suggesting a similar importance of autophagy across different oligodendroglial populations. Despite the loss of Atg7 in peripheral white matter, myelination was unaffected (Figures S1Q–S1S), consistent with previous reports indicating that macroautophagy is not required for myelin remodeling by Schwann cells (Brosius Lutz and Barres, 2014; Gomez-Sanchez et al., 2015; Jang et al., 2016).

We next examined how g-ratios change during adulthood. Analyses revealed that although myelin sheath thickness remains relatively unchanged from 2 to 16 months in controls, the thickness changed steeply with disruption of macroautophagy (Figure 1J). This indicates that OLGs maintain their myelin sheath thickness continuously through a balance of synthesis and macroautophagy-mediated degradation. Moreover, this supports the hypothesis that disruption of macroautophagy in OLGs precludes proper remodeling of CNS myelin *in vivo*.

Autophagosome formation and maturation can occur throughout the mature OLG

To confirm that increased myelin thickness over time is driven by continuous myelin remodeling rather than an increased demand for autophagic activity across time, we examined the presence of autophagosomes in Olig2^{+} cells in the corpus callosum of mice as a proxy for autophagic drive (Figures 2A and 2B). Adult mice transgenically expressing the autophagosome marker MAP 1A/1B-light chain 3 (LC3) tagged with GFP (GFP-LC3) (Mizushima et al., 2004) were treated acutely with chloroquine to slow the turnover of autophagosomes. We found that puncta intensity did not greatly change as mice aged and, if anything, decreased, suggesting that the relative reliance on oligodendroglial autophagy across time is fairly constant, and autophagic degradation of the myelin sheath may occur continuously in these cells.

In tissue, autophagosomes were most reliably visualized in oligodendroglial soma; thus, to gain a better spatial and mechanistic understanding of how macroautophagy remodels individual myelin sheaths, we isolated OPCs via immunopanning and induced their differentiation and maturation (Figures S2A and S2B) (Zuchero et al., 2015). Immunofluorescence against Atg16 (an indicator of autophagosome biogenesis) (Fujita et al., 2008), p62, and LC3 revealed that these proteins are expressed during all stages of oligodendroglial development (Figures 2C–2H and S2A–S2C), consistent with previously reported data (Bankston et al., 2019). Importantly, in mature OLGs, these autophagy markers are expressed in the cell body and throughout the cytoplasmic channels of the myelin sheath (Figures 2D, 2F, and 2H). To confirm that autophagosomes could form within these cytoplasmic channels, we asked whether a known source of autophagosome membrane was present there. Immunofluorescence for the integral endoplasmic reticulum (ER) membrane protein calnexin corroborates previous findings suggesting the presence of the ER throughout the mature OLG (Simpson et al., 1997) and indicates that a potential membrane source for autophagosome biogenesis (Hayashi-Nishino et al., 2009) is present in the myelin sheath's cytoplasmic channels (Figure S2C).

Given that macroautophagy is a multi-step, processive event, we next performed live-cell spinning disk confocal microscopy of mature GFP-LC3^{+} OLGs in culture. Cells were monitored and analyzed for the appearance of *de-novo*-formed autophagosomes, their acidification (via LysoTracker red positivity), and their disappearance. We observed regional heterogeneity in macroautophagic activity and therefore devised a nomenclature to describe substructures within the network of cytoplasmic channels (Figure 3A; Video S2): Arteries are large channels that may correspond to the outer and paranodal loops of the myelin sheath; branches are small channels that may correspond to intramyelinic cytoplasmic nanochannels (Snaidero et al., 2014, 2017); edges are channels that may correspond to the inner loop; and bulbs are enlargements within channels, often found at the distal ends of arteries.

Although autophagosomes showed both anterograde and retrograde movement as they acidified, in contrast to neurons (Maday and Holzbaur, 2012), the vast majority of structures remained stationary throughout formation and acidification (Figures 3B–3D and S3A; Video S3). Autophagosomes formed and acidified throughout the cell, and the majority were present within channels within the myelin sheath, appearing at especially high frequency

in artery-branch intersections and bulbs (Figures 3E and S3B). In addition, the time until acidification of structures varied modestly by subcellular region and correlated with distance from the cell body with those closer acidifying slightly faster (Figures 3F and S3C). Taken together, our data indicate that autophagosome biogenesis and maturation can occur throughout the mature OLG, including within the cytoplasmic channels of the myelin sheath.

MBP is a cargo for selective autophagy

We next sought to identify the myelin proteins captured by macroautophagy. MBP is an essential cytosolic component of the myelin sheath (Boggs, 2006). Modest lysosomal inhibition caused MBP to accumulate and co-localize with endogenous LC3 and LAMP2, consistent with it being an autophagic cargo (Figures 4A, S4A, and S4B). We next created macroautophagy-deficient OLGs to pursue this further. We turned to *Atg5* deletion so that we can monitor Cre activity through expression of a TdTomato reporter (*Atg7* is on the same chromosome as the *Rosa26* locus) (Madisen et al., 2010). Using this approach, we found that *CNP^Cre* was active in the isolated OPCs (Figures S4C and S4D). Consistent with our *in vivo* findings with *Atg7* deletion (Figure S1), the loss of *Atg5* inhibited autophagy (Figures 4B and 4C) and, in contrast to previous reports (Bankston et al., 2019), had no noticeable impact on OLG differentiation *in vitro* (Figures S4C–S4E). Immunoblotting of OLG lysates revealed that the absence of Atg5 caused MBP to accumulate in the detergent-insoluble pool with increased laddering, suggestive of MBP aggregation (Figure 4D). MBP levels were also higher in the corpus callosum of adult Atg5cKO mice, similar to Atg7cKO mice, and extended into the cortical layers (Figures 4E and 4F), consistent with observations in TFEB mutant mice (Sun et al., 2018). In culture, co-staining for p62 and MBP confirmed not only that MBP+ inclusions were present but that many of them were also positive for p62 (Figures 4G and 4H). Given that MBP is an intrinsically disordered protein (Boggs, 2006) that has a high propensity toward aggregation (Frid et al., 2015; Riccio et al., 1995) and that p62 is implicated in aggregate turnover by macroautophagy (Pankiv et al., 2007), we next tested the hypothesis that MBP and p62 co-localize because MBP is degraded by selective autophagy.

Selective autophagy is the means by which autophagic cargoes are trafficked for degradation in an adaptor protein-dependent manner to permit selective cargo (Lynch-Day and Klionsky, 2010). Different cargoes can be degraded selectively, such as mitochondria (mitophagy), invading pathogens (xenophagy), and aggregated proteins (aggrephagy). In aggrephagy, the adaptor protein WDFY3 (also known as autophagy-linked FYVE protein [Alfy]), works with p62 to degrade aggregated proteins by autophagy (Filimonenko et al., 2010; Fox et al., 2020). Co-immunoprecipitation experiments of MBP from white matter in wild-type (WT) mice revealed that MBP is in a complex with p62, Alfy, and LC3 forms I and II (Figure 4I). Ultrastructural studies of OLGs with mild lysosomal inhibition revealed the presence of electron-dense aggregates within double membrane structures devoid of bulk cytosol (Figure 4J), a hallmark of cytoplasm to vacuole targeting, the yeast paradigm of mammalian aggrephagy (Lynch-Day and Klionsky, 2010). These data reinforce the observation that MBP is degraded in an Alfy-dependent manner consistent with selective autophagy.

Integral membrane myelin proteins require macroautophagy for their degradation

As with MBP, immunofluorescence revealed that lysosomal inhibition increased accumulation of transmembrane myelin proteins such as proteolipid protein (PLP) and myelin OLG glycoprotein (MOG) (Figures 5A and 5B) and increased their co-localization with LC3^{+} structures (Figures 5C and S5A; data not shown), suggesting that macroautophagy is required for their degradation. To pursue this hypothesis further, we performed density gradient centrifugation of homogenates from adult WT brains to enrich for autophagic vacuoles (AVs) (Fox et al., 2020; Stromhaug et al., 1998) (Figure 5D). Immunoblotting of the recovered fractions revealed that MBP, MOG, PLP, and myelin-associated glycoprotein (MAG) fractionated into the AV fraction (Figure 5E; data not shown), and into the expected, myelin-enriched light membrane fraction (Figure S5B; data not shown). To further enrich the AV fraction away from potential ER microsomes and endocytic structures, we next immuno-isolated fraction F5 for vesicles positive for LC3 (Figure 5D) (Jeong et al., 2009). Immunoblotting revealed that immuno-isolation further enriched the fraction for myelin proteins (Figure 5F). Moreover, proteinase K (PK) protection assays confirmed that MBP, MOG, MAG, and PLP are internalized within autophagosomes along with p62 (Figure 5G). Taken together, these data strongly suggest LC3^{+} autophagic structures capture integral myelin membrane proteins. The PK protection assay also further strengthened the hypothesis that MBP within AVs is in highly ordered structures: in the absence of detergent, novel MBP[+] bands appeared in a PK dose-dependent manner (Figures S5C and S5D), indicating the presence of detergent- and PK-resistant aggregates of MBP within the AVs. Taken together, these data are consistent with the observation that macroautophagy degrades the cytosolic and integral membrane components of the myelin sheath.

The amphisome brings together the cytoplasmic and integral membrane components of myelin to permit their degradation by the lysosome

We next examined the origin of the integral myelin membrane proteins found in the AVs via immunofluorescence (Figure 5). Given that these cell-surface proteins must be first internalized by endocytosis, these data suggest they are brought to LC3^{+} structures through the formation of an amphisome (Berg et al., 1998; Stromhaug and Seglen, 1993). Amphisomes form by fusion of endocytic vesicles with nascent autophagosomes and may consolidate cargoes prior to lysosome-mediated degradation in the soma, especially in neurons (Hollenbeck, 1993; Maday and Holzbaur, 2012; Yamamoto and Simonsen, 2012). In WT OLGs, a subset of structures positive for mCLING—a fluorescently tagged fixable probe that labels the plasma membrane (Revelo et al., 2014)—co-localized with LC3, similarly to MOG (Figure 5C), strongly supporting the hypothesis that amphisome formation was occurring in OLGs (Figure S6A). Similarly, immunofluorescence revealed that mCLING[+]MOG[+] structures in control (Ctrl) cultures co-localized with MBP, indicating that when autophagy was intact, the endocytosed and cytosolic cargoes could arrive to the same vesicle structure (Figures 6A and 6B). Ultrastructural studies of Ctrl OLGs also revealed the presence of amphisome-like structures carrying myelin-like cargo: structures that resembled double-membrane vesicles that had fused with single-membrane vesicles filled with myelin-like membranes (Figure 6C). Unilamellar structures filled with electron

dense material and membranous structures suggestive of the autolysosome were also identified (Figure 6D).

Although the internalization of mCLING$^+$MOG$^+$ structures was observed throughout the OLG in Atg5 Ctrl and conditional knockout (cKO) cultures (Figures 6A and 6B), MOG and PLP accumulated throughout the cell in Atg5cKO OLGs (Figures 5A and 5B). mCLING$^+$MOG$^+$ vesicles rarely co-localized with endocytic cargo such as transferrin receptor (TfR) (Figures S6B and S6C), which did not accumulate in Atg5cKO cells (data not shown). This is consistent with data in immortalized cells suggesting that integral membrane myelin proteins do not undergo constitutive endocytosis like TfR (Winterstein et al., 2008). Taken together, these data suggest that despite internalization via endocytosis, the integral myelin membrane proteins still require autophagy for degradation. Given that the myelin membrane is especially rich in cholesterol and sphingolipids, and proteins such as PLP are cholesterol interacting (Simons et al., 2000), the amphisome may allow structures internalized in a clathrin-independent manner to reach the lysosome.

To examine this further, we returned to live-cell imaging of GFP-LC3$^+$ OLGs to capture amphisome formation through the fusion of GFP-LC3$^+$ autophagosomes with mCLING$^+$ endosomes (Figures 6E–6G, S4D, and S4E; Videos S4 and S5). Incubation with mCLING led to a broad distribution of mCLING$^+$ structures throughout the cell, comparable to the distribution of GFP-LC3$^+$ vesicles, although greater in number. In addition, we observed GFP-LC3$^+$ vesicles fusing with mCLING$^+$ structures throughout the cell, with an average of about 13% of GFP-LC3 vesicles showing this fusion event. A summary of the data is presented in Figure 6G. These data demonstrate that amphisomes form in OLGs and can thereby traffic integral membrane proteins to the autophagosome. Our data suggest a model in which the amphisome allows for the coordination of autophagy and endocytosis that is required for efficient lysosome-mediated degradation of this complex and highly specialized adaptation of the myelin sheath (Figure S6F).

Inactivation of macroautophagy in OLGs leads to behavioral dysfunction, neurodegeneration, and premature lethality

We found that the loss of oligodendroglial macroautophagy prevents the turnover of myelin sheaths in the adult brain, leading to thickening of the myelin sheath as the animal ages (Figure 1). Consistent with an aging-related phenotype, although neither the Atg7cKO nor Atg5cKO mice showed signs of developmental deficits (Figure S1), as they matured, began to develop tremors and motor deficits and then died prematurely, starting at approximately 8 months old (Figures 7A–7C; Videos S1 and S6). Immunofluorescence revealed that the cortices from aged autophagy-deficient mice contained aggregation of myelin proteins, myelin degeneration, and glial degeneration (Figures 7D–7G, S7A, and S7D). At the ultrastructural level, myelin debris and aberrant myelin sheath morphologies, including abnormally enlarged and displaced inner loops, were also prevalent (Figure 7I; Ctrl: 3.4 $\pm$ 2.0/1,000 μm^2 versus Atg7cKO: 30.8 $\pm$ 11.7/1,000 μm^2). Many of these ultrastructural abnormalities have been previously shown to disrupt axon conduction (Patzig et al., 2016), which may explain why motor symptoms developed. Aberrant myelin sheath morphologies were often accompanied by the presence of axonal spheroids (Figure 7I), a sign of axonal

degeneration. Neuronal death was also evident in these brains, as demonstrated by the presence of activated caspase-3 in neurons of aged Atg7cKO (Figures 7G and 7H) and Atg5cKO (Figure S7E) mice, which is quite notable given that Cre was expressed in the callosum but not ectopically in cortical regions (Figures S7B and S7C). Hemispheric volumetric measurements suggest that these degenerative effects were not caused by compression within the calvarium (Atg5 Ctrl: $3.85e^{10}$ μm^3 versus Atg5cKO $3.82e^{10}$ μm^3; Student's t test, p = 0.817). Taken together, these data strongly suggest that the loss of the ability to regulate myelin sheath thickness through amphisome-coordinated degradation disrupts neural circuitry leading to behavioral deficits and, ultimately, death.

DISCUSSION

In this study, we found that OLGs have adapted macroautophagy to degrade and maintain their preexisting myelin sheaths and that this remodeling is essential for maintaining a healthy CNS. We determined that disruption of oligodendroglial macroautophagy *in vivo* led to an age-dependent increase in myelin thickness and abnormal myelin structures, which resulted in neuronal and glial degeneration and death. Further examination in culture indicated that macroautophagy is necessary for the efficient degradation of cytoplasmic and integral membrane myelin proteins, which come together through the formation of an amphisome intermediate prior to lysosome-mediated degradation.

Our live-cell imaging studies indicate that the turnover of myelin components can occur throughout the myelin sheath, which suggests that myelin turnover may occur locally in a manner coordinated with the creation of new myelin. Studies have raised the possibility that mature OLGs may modulate the thickness of their myelin sheaths by reinitiation of myelin growth (Goebbels et al., 2010; Jeffries et al., 2016; Snaidero et al., 2014; Yeung et al., 2014). Indeed, we find that over time, the g-ratio remains fairly steady in healthy Ctrl animals, suggesting that the induction of myelin growth leads to increased myelin thickness along with redundant myelin, similar to our observations in Atg7(CNP) cKO brains (Goebbels et al., 2010; Ishii et al., 2016; Snaidero et al., 2014). These data indicate that myelin growth and degradation are in a delicate balance, the mechanism of which remains under further study. Notably, our studies revealed both *in vivo* and *in vitro* that neither Atg5 nor Atg7 are essential for OLG differentiation. A recent study, however, found acute depletion or functional interference of Atg5 was essential for OLG maturation (Bankston et al., 2019). In addition to macroautophagy, this may reflect the non-canonical pathways in which Atg5 are implicated (Ye et al., 2018), especially secretion and cell death.

The accumulation of the myelin sheath, though time-dependent, might be less of a function of absolute age but rather a reflection of the rate of sheath formation. Suggestive of a continuous cell-autonomous myelin remodeling process, we observed a gradual, yet progressive, increase in myelin thickness over time in the absence of macroautophagy. This is consistent with the known observation that myelin-associated proteins and lipids have some of the longest half-lives of any structure in the CNS (Fischer and Morell, 1974; Savas et al., 2012). Moreover, our data strongly suggest that the degradation occurs throughout life, especially during reproductive ages of 2–9 months old (Figure 1), and then slows with advanced age (16 months old), similar to the lysosome-mediated degradative capacity

upon which macroautophagy depends (Cuervo and Dice, 2000). Conditional approaches that disrupt oligodendroglial autophagy in a temporally regulated manner might better address this question. Indeed, we find that degradation occurs across the lifespan; autophagosomes isolated from WT brains as early as 3 to 14 months old unfailingly contained proteins such as MBP and MOG (Figures 5D–5G). When lysosome-mediated degradation begins to fail, such as in the aging animal (Safaiyan et al., 2016) or after CNS injury (Baumann and Pham-Dinh, 2001), non-cell autonomous events also contribute to myelin turnover.

The amphisome intermediate is an under-studied element of autophagic degradation. Our findings suggest that cells have evolved an additional fusion step in autophagy to increase the adaptability of lysosome-mediated degradation and accommodate the needs of highly specialized cells. Specifically, we found that degradation of cholesterol- and sphingolipid-enriched endocytic cargo transits through autophagy and the amphisome for lysosome-mediated degradation. A significant question raised by our observations is why endocytosed myelin-associated proteins and membranes need to traffic through the amphisome to be degraded efficiently. In neurons, amphisome formation had been suggested to form out of efficiency, as retrograde transport is required for all axonal proteins to be degraded by lysosomes (Fu et al., 2014; Maday and Holzbaur, 2014; Maday et al., 2012), which are concentrated at the soma (Ferguson, 2019; Yap et al., 2018). OLGs, although similarly large and highly compartmentalized as neurons, still require amphisome formation, despite the ability to degrade locally autophagic contents (Figures 2 and 3). Our data suggest that in OLGs, the degradation of myelin requires local coordination of the cytoplasmic and membranous components to ensure appropriate degradation. The efficiency of this degradation would permit local coordination with myelin synthesis during renewal and remodeling in the distal tip of the myelin sheath (Lyons et al., 2009; Wake et al., 2011). Another important consideration is the composition of myelin membranes, which are particularly rich in cholesterol and sphingolipids. These endocytosed vesicles may require an alternative compartment to reach the lysosome. For OLGs, and possibly other cells that internalize substrates in a clathrin-independent manner, fusion with autophagosomes may provide the alternative route to the lysosome.

Changes in OLG health are common across age-related neurodegenerative diseases (Huang et al., 2015; Mathys et al., 2019; Strohm and Behrends, 2019). Given that macroautophagy has been similarly implicated (Griffey and Yamamoto, 2022), and that lysosome-mediated degradative capacity declines with age (Cuervo and Dice, 2000), our data suggest a possible mechanism linking macroautophagy dysfunction and oligodendroglial health in neurodegenerative disease. Moreover, the implication that MBP is degraded in an Alfy-dependent manner raises the question of whether its degradation becomes compromised, as protein aggregation due to independent disease processes ensue. Nonetheless, further studies examining the importance of OLG health and macroautophagy dysfunction in disease are necessary. For example, in multiple sclerosis, autophagic dysregulation might continuously compromise myelin sheath integrity, even that of newly formed myelin sheaths, thereby contributing to both primary and secondary progressive stages of disease. Our data showing that myelin components can be consolidated for selective autophagic degradation, linking macroautophagy with myelin sheath remodeling, also imply that changes in macroautophagy could underlie circuitry dysfunction known to occur in the absence of neuronal loss across

neurodegenerative diseases, such as Alzheimer disease (AD). Small changes in myelin sheath thickness may have profound effects on neuronal network function and have a major impact on sensory adaptation (Pajevic et al., 2014; Smith and Koles, 1970). Similarly, the disruption of saltatory conduction and changes in intracellular calcium might disrupt axonal trafficking, and alterations in the myelin sheath may impair the OLG's ability to provide metabolic support to axons (Funfschilling et al., 2012; Lee et al., 2012). Strikingly, the behavioral deficits and myelin sheath accumulation in autophagy-deficient mice preceded neuronal and glial degeneration. This strongly suggests that disruption of myelin remodeling and adaptive timing of action potentials may not only cause neurodegenerative processes but also contribute to disorders in which asynchronous neuronal firing causes dysfunction, such as epilepsy, schizophrenia, and dyslexia (Fields, 2008; Filley and Fields, 2016; Pajevic et al., 2014).

Taken together, our study indicates that as we consider how macroautophagy dysfunction might contribute to neurodegeneration in disease states, we must gain better insight into how this intracellular event maintains the homeostasis of the discrete, varied, and highly adapted cell types of the CNS. Here, we show how OLGs use this pathway to meet their unique needs and how the disruption of this pathway can have cell-autonomous and non-cell-autonomous consequences. Moreover, the demonstration that the myelin sheath of the adult brain can be degraded cell autonomously allows for new considerations in how potential changes in the myelin sheath might influence the formation and maintenance of neural circuits.

Limitations of the study

In this study, we assessed the consequences of disrupted OLG macroautophagy on myelin and CNS health. Considering the broad pathological findings, our focus on ultrastructure in key white matter areas and the most prominent behavioral dysfunction leaves open the possibility that these mice exhibit subtle defects in other brain regions, with corresponding cellular and organismal phenotypes. Although this study supports a role for oligodendroglial macroautophagy in the maintenance of myelin for proper CNS health, our insight into the physiological failure experienced by both OLGs and the neurons they support remains limited. For example, we do not know at an electrophysiological level how these abnormal myelin structures impair neurotransmission. Additionally, our data suggest an interaction between myelin synthesis and macroautophagy-mediated degradation across time, the precise nature of which requires further study.

STAR★METHODS

Detailed methods are provided in the online version of this paper and include the following:

RESOURCE AVAILABILITY

Lead contact—Further information and requests for reagents may be directed to and will be fulfilled by the Lead Contact, Ai Yamamoto (ai.yamamoto@columbia.edu).

Materials availability—This study did not generate new unique reagents.

Data and code availability

- All data reported in this paper will be shared by the lead contact upon request.

- This paper does not report original code.

- Any additional information required to reanalyze the data reported in this paper is available from the lead contact upon request.

EXPERIMENTAL MODEL AND SUBJECT DETAILS

Mice—All animals and procedures complied with the Guide for Care and Use of Laboratory Animals and were approved by the IACUC committee at Columbia University. Mice were maintained in a 12h/12h light/dark cycle in a temperature and humidity-controlled environment, with ad libitum access to food and water. Previously created CNP-Cre (Lappe-Siefke et al., 2003), Atg7-floxed (Komatsu et al., 2005), Atg5-floxed (Hara et al., 2006), GFP-LC3 (Mizushima et al., 2004), and TdTomato/Ai9-reporter (Madisen et al., 2010) mouse lines were maintained by breeding with C57BL/6 mice. All experiments with mice were performed and analyzed blindly without knowledge of their genotype. We observed no sexual dimorphism of myelination in mice, so males and females were pooled for all analyses, except for behavior, which was powered and performed assuming sex would be an independent variable. cKO mice were compared to cHet mice because heterozygous loss of CNP through CNP^{Cre} knock-in has been suggested to have a mild behavioral phenotype in 26 month-old mice (Hagemeyer et al., 2012).

Primary cultures—All cells were cultured at 37°C under 5% CO_2 in serum-free defined media containing DMEM, transferrin (100 μg/mL), BSA (100μg/mL), putrescine (16 μg/mL), progesterone (60 ng/mL), sodium selenite (40 ng/mL), N-acetyl-L-cysteine (5 μg/mL), d-biotin (10 ng/mL), forskolin (4.2 μg/mL), insulin (5 μg/mL) (all from Sigma), glutamine (2 mM), sodium pyruvate (1 mM), B27 (2%), penicillin–streptomycin (100 U/mL) (all from Invitrogen), Trace Elements B (1x, Cellgro), and LIF (20 ng/mL, Chemicon). Proliferation medium also contained OPC mitogens PDGF-AA (20 ng/mL) and NT-3 (1 ng/mL) (both from PeproTech), while differentiation medium contained triiodothyronine (40 ng/mL, Sigma) without OPC mitogens. For experiments in which only mature OLGs were examined (and not any intervening stages of differentiation), the differentiation medium was modified by using DMEM/F12 base media (Invitrogen) and a higher dose of insulin (25 μg/mL) to maximize OLG survival.

METHOD DETAILS

Reverse transcription polymerase chain reaction (RT-PCR)—Total RNA was isolated from whole brains with TRIzol reagent (ThermoFisher). First-strand cDNA synthesis from mRNA was performed using the AMV Reverse Transcription System (Promega) with Oligo(dT)$_{12-18}$ primers. Products were amplified using template-specific primers listed in the Key resources table (Lebrun-Julien et al., 2014) and semi-quantitatively analyzed by gel electrophoresis.

Open field testing—At least one week before starting behavioral testing, experimental mice were relocated to a reverse-cycle core facility with the lights off between 10 AM

and 10 PM, so that experiments could be performed during the dark phase (i.e. the mice's active phase). Power analyses based on pilot data were used to establish the number of mice required to have 90% power to reach 95% confidence. Figure S1: Male mice were placed inside an open field arena (43.2 cm × 43.2 cm × 30.5 cm) for 60 min at two m/o. Figure 7B: Male mice were placed for 5 min at 2, 5 and 8 m/o. Figure 7C: A mixed sex cohort of mice were placed for 60 min at 12 and 16m/o. Only rearing was measured in this cohort, given the limited size of the cohort. Measurements of distance traveled and number of rearings were recorded and measured using equipment and software from Med Associates.

Immunohistochemistry—Mice were deeply anesthetized with isoflurane and transcardially perfused with 0.9% saline followed by 4% paraformaldehyde (PFA). Brains were dissected, fixed in 4% PFA for 1 h at room temperature and then 4°C overnight, cryoprotected in 30% sucrose in phosphate buffer at 4°C, snap-frozen in powdered dry ice, embedded in O.C.T. Compound (Fisher), and stored at −80°C. Free-floating brain cryosections (30 or 50 μm) were cut on a cryostat and stored at 4°C in phosphate buffer containing 0.02% sodium azide. For antigen retrieval, sections were placed at 80°C in 10mM sodium citrate (pH = 9.0). Sections were permeabilized with 0.4% Triton and blocked with 10% BSA in PBS, and then incubated in primary antibody diluted in PBS 0.01% Triton X-100 overnight at 4°C (when staining for NG2, sections were left in primary antibody for three nights) (see Key resources table for a list of antibodies). Sections were subsequently incubated in Alexa Fluor conjugated secondary antibodies (Life Technologies) diluted in 0.01% Triton X-100 PBS for 1 to 2 hs at room temperature, stained with either Hoechst (Invitrogen) for 10 min after or NeuroTrace blue-fluorescent Nissl stain (ThermoFisher) during secondary incubation, mounted onto glass slides, and coverslipped using Prolong Gold antifade reagent (Life Technologies).

For staining of oligodendroglia in cortex (Figure 7), all brains were perfused and post-fixed in 4% PFA and stored in PBS. Brains were sectioned coronally at 75 um thickness using a vibratome (Leica VT 1000 S) at room temperature in PBS. Sections were collected and maintained in wells filled with 0.1% sodium azide in PBS at 4°C. To immunostain, each section was subjected to heat-induced antigen retrieval in 50mM sodium citrate (0.05% Tween 20, pH6) for 26 min at 95 C. Sections were then cooled on bench to room temperature (20 min), blocked 2 h in 0.1% Triton X- and 5% NGS in PBS, and incubated for 1–3 days as needed in 0.1% Triton X- and 5% Normal Goat Serum (NGS) in PBS at 4C with the following primary antibodies:

- pM_CNPase (Biolegend; Cat# 836,404; 1:1000)

- pC_NFH-H (Encor Cat# CPCA-NF-H; 1:500)

- pRb_NeuN (Abcam, Cat# ab177487; 1:500) for 9 and 12-month mice only

Sections were then incubated for 1 day in 0.1% Triton X- and 5% NGS in PBS at 4C in AlexaFluor Fluorescent Secondary Antibodies of the appropriate corresponding host species at 1:600 dilution, then in DAPI (2.5 μg/mL) and finally mounted onto glass slides in diluted mounting media (Dako Ultramount, Cat# S1964; diluted 1:4 in PBS) and imaged using Leica SP5 upright confocal laser scanning microscope (40X water immersion objective).

The same group of laser and image detector configurations was used to collect each image throughout each experimental dataset.

Cell counting—Every eighth serially-cut coronal brain sections of 2m/o brains were used for all cell counting. Matching sections from 1.10 mm to –0.82 mm bregma were used to count NG2+ and Olig2+, CC1+ cells in the corpus callosum. Unbiased counts were obtained using NIH ImageJ. For NG2+ cells, pericytes were excluded based on their morphology.

Electron microscopy—Transmission electron microscopy was performed in conjunction with the Electron Microscope Facility at Columbia University Medical Center. Briefly, mice were deeply anesthetized with isoflurane and transcardially perfused with 0.9% saline followed by 2.5% glutaraldehyde, 2% PFA in 0.1 M sodium cacodylate buffer (pH = 7.2). Optic nerves, corpus callosi, sciatic nerves, and spinal cords were dissected, post-fixed in 2.5% glutaraldehyde, 2% PFA in 0.1 M sodium cacodylate buffer for 1 h at room temperature and then 4°C at least overnight. Tissue was then postfixed with 1% OsO4 also in Cacodylate buffer for one h. After dehydration tissue was embedded in Lx-112 (Ladd Research Industries, Inc.).

A similar procedure was employed for cultured oligodendrocytes. Cells were fixed with 2.5% glutaraldehyde in 0.1M Sorenson's buffer (PH 7.2) for at least one h. Cells were then post-fixed with 1% OsO4 also in Sorenson's buffer for one h. After dehydration cells were embedded in a mixture of Lx-112 (Ladd Research Industries, Inc.) and Embed-812 (EMS, Fort Washington, PA).

For both tissue and cells, thin sections were cut on the PT-XL ultramicrotome at 60nm thick. The sections were stained with uranyl acetate and lead citrate and examined under a JEOL JEM-1200 EXII electron microscope. Images were captured with an ORCA-HR digital camera (Hamamatsu) and recorded with an AMT Image Capture Engine.

All imaging and analysis were conducted blinded to the experimental condition. For measuring g-ratios, 75 axons per animal were scored. For measuring percent axons myelinated in the corpus callosum, approximately 250 axons per animal were scored. Morphological features were identified manually, and NIH ImageJ was used to measure dimensions of interest.

Evaluation of basal autophagy *in vivo*—GFP-LC3 transgenic mice (2, 9, and 12 months of age) were treated with chloroquine (100 mg/kg) by intraperitoneal injection 2 h prior to sacrifice. In each corpus callosum, 50–100 Olig2+ cells were evaluated by quantifying the raw integrated density (NIH ImageJ) of GFP-LC3 signal in the soma at the mid-nuclear level, correcting for measured area (perinuclear of Olig2 positive cells).

Lysis of brain tissue—Mice were deeply anesthetized with isoflurane and decapitated. Brains were removed and placed into 1 mL Eppendorf tubes. Samples were flash-frozen on powdered dry ice and stored at –80°C until processing. Brains were placed in a glass Dounce homogenizer with an equivalent volume of 1x PBS containing Halt protease inhibitor cocktail (ThermoFisher) and disaggregated with 20 pumps of the pestle. The

suspension was transferred to a tube and an equal volume of detergent (2% Triton X-100 in PBS) was added. After 30 min on ice, samples were spun in an Eppendorf 5417R centrifuge at 2,000 g for 5 min at 4°C. The supernatant was transferred to another tube for use in future experiments.

Isolation of autophagic vacuoles (AVs)—Nycodenz cell fractionation methods were performed as previously described (Fox et al., 2020). Briefly, mice were deeply anesthetized with isoflurane and decapitated. Brains were removed, mechanically disrupted, and fractionated using a discontinuous Nycodenz gradient (Stromhaug et al., 1998). Isolated fractions were then examined by immunoblotting or further purified for LC3+ structures by immuno-isolation (Jeong et al., 2009). For immuno-isolation, 30 µg of the AV fraction were incubated with 4 µg of rabbit anti-LC3A/B (Abcam) in 1x sucrose-HEPES buffer with Halt protease inhibitor cocktail (ThermoFisher) and without detergent overnight at 4°C. Subsequent immune-vesicle structure complexes were incubated with Protein A MicroBeads (Miltenyi Biotec) for 1 h at 4°C and isolated using µ columns (Miltenyi Biotec).

Co-immunoprecipitation—6 m/o adult mice were pre-treated with chloroquine (50 mg/kg) by intraperitoneal injection for 7 days then sacrificed. Brain lysate (30 µg) was incubated with 4 µg of rat anti-MBP (Bio-Rad) overnight at 4°C. Immune-protein complexes were incubated with Protein G MicroBeads (Miltenyi Biotec) for 1 h at 4°C and isolated using µ columns (Miltenyi Biotec). MBP pulldown was first evaluated by immunoblotting using mouse anti-MBP (Covance).

Proteinase K (PK) protection assay—Isolated AV fractions (30 µg) were incubated with 0, 0.1, or 1.0 µg of proteinase K (Sigma) for varying lengths of time in the absence or presence of 0.2% Triton X-100 in 1x sucrose-HEPES buffer at room temperature. Reactions were stopped by incubating samples in 10 mM phenylmethylsulfonyl fluoride (PMSF, Sigma) for 10 min at room temperature followed by flash freezing in liquid nitrogen, and samples were analyzed by immunoblotting.

Purification of cells—OPCs were purified from enzymatically dissociated P6–8 C57BL/6 or transgenic mouse cortices by immunopanning and grown in serum-free defined medium, as described previously with minor modifications (Emery and Dugas, 2013). Briefly, tissue was diced and digested in papain (Worthington) at 37°C for 90 min and then gently dissociated. Dissociated cortices were sequentially immunopanned on BSL1 (Vector Laboratories) and then O4 antibody-coated plates to select for O4+ OPCs. After rinsing nonadherent cells away, purified OPCs were removed from the final panning plate with trypsin and transferred to poly-D-lysine coated tissue culture dishes.

Immunocytochemistry—After the appropriate number of days of differentiation, cells were fixed immediately or treated with either leupeptin (Sigma) for 2 h or mCLING (Synaptic Systems) overnight through a half media change before fixation. Cells were fixed for 10 min with 4% paraformaldehyde, permeabilized in 0.01% Triton X-100 in PBS, blocked in 10% BSA in PBS and stained with primary antibodies diluted in 0.01% Triton X-100 in PBS overnight at 4°C or for 1 h at room temperature (see Key resources table for a list of antibodies). Alexa Fluor conjugated secondary antibodies (Life Technologies) were

diluted in 0.01% Triton X-100 PBS, incubated with coverslips for 1 h at room temperature, and mounted with Prolong Gold antifade reagent with DAPI (Life Technologies) onto glass slides.

Live-cell imaging of OLGs—OPCs were plated on poly-D-lysine-coated glass bottom imaging dishes (35 mm, MatTek) and differentiated for 10–11 days as above. Prior to imaging, cells were incubated for 60 min at 37°C in DMEM with LysoTracker red DND-99 (75 nM, Invitrogen) or overnight at 37°C in DMEM with mCLING-Alexa Fluor 594, then washed once with and imaged in warm Hibernate A media (Invitrogen) to reduce phototoxicity. mCLING was prepared for live imaging by conjugating unlabeled mCLING with Alexa Fluor 594 C5 Maleimide (ThermoFisher) using an mCLING labeling kit (Synaptic Systems). Cells were imaged using a spinning disc confocal unit (CSU-10; Yokogawa Electric Corporation) with Borealis (Spectral Applied Research) on an inverted microscope (Ti; Nikon) with a charge-coupled device camera (Orca-R2; Hamamatsu Photonics). Z-sectioning was done with a Piezo-driven motorized stage (Applied Scientific Instrumentation), and focus was maintained using Perfect Focus (Nikon) before each z series acquisition. An acousto-optic tunable filter was used to select the excitation light of two 100 mW lasers for excitation at 491 and 561 nm for eGFP and LysoTracker/mCLING, respectively (Spectral Applied Research), and a filter wheel was used for emission wavelength selection (Sutter Instruments). The system was controlled by MetaMorph software (Molecular Devices). Temperature was maintained at 37°C using an air stream stage incubator (Nevtek). 4×0.75 μm Z sections were acquired every 60 s for at least 60 min using a 60×1.4 N.A. oil immersion PlanApochromat objective lens, with 2×2 binning.

ImageJ (Schneider et al., 2012) was used for all data analysis. Maximum intensity projections of GFP-LC3 and LysoTracker/mCLING were generated for each frame. To remove static features, we subtracted a minimum projection of all the time points from each frame. Identification of puncta and area measurements was performed by hand using ImageJ. Image analyses were performed on still images by tracing and measuring puncta and cell contours using ImageJ.

Fluorescence microscopy—A Leica SP5 confocal microscope was used to image both fixed OLG cultures and fixed brain sections. When necessary, confocal Z-stacks were taken every 0.45 μm.

Immunoblotting—Whole cell lysates and tissue lysates from freshly frozen dissected brain were generated using 1% Triton X-100 in PBS containing Halt protease inhibitor cocktail (ThermoFisher). All samples were cleared by centrifugation at 2,000 g for 5 min at 4°C. Cell lysates were subjected to an additional centrifugation step of 21,000 g for 10 min, the pellet of which was resuspended in 8 M Urea in PBS with 1% Triton X-100 and protease inhibitor. Protein concentration was determined using the DC Protein Assay (Bio-rad Laboratories [Hercules, CA]) and equal amounts of protein (1–20 μg) were prepared and loaded onto 4–12% Bis-Tris and blotted to PVDF membranes as described by the manufacturer's recommendations (Life Technologies). PVDF membranes were blocked in 3% BSA in PBS containing 1% Tween 20. Antibodies were incubated overnight at 4°C (see Key resources table for a list of antibodies). The appropriate HRP-conjugated secondary

antibodies (ThermoFisher Scientific) were diluted in 1% BSA PBS and a chemiluminescent reaction (West Dura SuperSignal, ThermoFisher Scientific) was detected by the Versadoc Imaging System (Bio-rad).

Brain volume assessment—To quantify brain volume, we used a modified version of the trapezoidal estimation of method of morphometric volume (Rosen and Harry, 1990). Between anterior and posterior anatomical landmarks in the forebrain, we obtained cross-sectional area measurements of hemispheres in serial sections, and summated segment volumes by approximating brain tissue as a conical frustum using the following equation:

$$V = \frac{1}{3}h\left(A_1 + A_2 + \sqrt{A_1 A_2}\right)$$

where h is the distance between serial sections and A1 and A2 are the cross-sectional areas of brain hemispheres in adjacent serial sections.

QUANTIFICATION AND STATISTICAL ANALYSIS

Statistical analyses were performed using Statview 5.0 (SAS Institute) or MATLAB (Mathworks). Statistical significance was accepted at $p < 0.05$. Normally distributed data were subject to student t-test or, for multiple comparisons, analysis of variance (ANOVA). Complete F-statistics and calculated p values are also available in the figure legends. Power analyses for behavioral studies were performed to achieve a power of 0.8 with a confidence of 0.95 using G*Power 3.1 (Faul et al., 2009). Effect sizes were based upon pilot studies, previously published, or unpublished materials. n-values are indicative of biological replicates and no data were excluded from analyses.

Supplementary Material

Refer to Web version on PubMed Central for supplementary material.

ACKNOWLEDGMENTS

REFERENCES

Aggarwal S, Yurlova L, and Simons M (2011a). Central nervous system myelin: structure, synthesis and assembly. Trends Cell Biol. 21, 585–593. [PubMed: 21763137]

Aggarwal S, Yurlova L, Snaidero N, Reetz C, Frey S, Zimmermann J, Pähler G, Janshoff A, Friedrichs J, Müller DJ, et al. (2011b). A size barrier limits protein diffusion at the cell surface to generate lipid-rich myelin-membrane sheets. Dev. Cell 21, 445–456. [PubMed: 21885353]

Bankston AN, Forston MD, Howard RM, Andres KR, Smith AE, Ohri SS, Bates ML, Bunge MB, and Whittemore SR (2019). Autophagy is essential for oligodendrocyte differentiation, survival, and proper myelination. Glia 67, 1745–1759. [PubMed: 31162728]

Baumann N, and Pham-Dinh D (2001). Biology of oligodendrocyte and myelin in the mammalian central nervous system. Physiol. Rev. 81, 871–927. [PubMed: 11274346]

Berg TO, Fengsrud M, Strømhaug PE, Berg T, and Seglen PO (1998). Isolation and characterization of rat liver amphisomes. Evidence for fusion of autophagosomes with both early and late endosomes. J. Biol. Chem. 273, 21883–21892. [PubMed: 9705327]

Boggs JM (2006). Myelin basic protein: a multifunctional protein. Cell. Mol. Life Sci. 63, 1945–1961. [PubMed: 16794783]

Brosius Lutz A, and Barres BA (2014). Contrasting the glial response to axon injury in the central and peripheral nervous systems. Dev. Cell 28, 7–17. [PubMed: 24434136]

Crang AJ, Gilson J, and Blakemore WF (1998). The demonstration by transplantation of the very restricted remyelinating potential of post-mitotic oligodendrocytes. J. Neurocytol. 27, 541–553. [PubMed: 11246493]

Crawford AH, Tripathi RB, Foerster S, McKenzie I, Kougioumtzidou E, Grist M, Richardson WD, and Franklin RJM (2016). Pre-existing mature oligodendrocytes do not contribute to remyelination following toxin-induced spinal cord demyelination. Am. J. Pathol. 186, 511–516. [PubMed: 26773350]

Cuervo AM, and Dice JF (2000). When lysosomes get old. Exp. Gerontol. 35, 119–131. [PubMed: 10767573]

Czopka T, Ffrench-Constant C, and Lyons DA (2013). Individual oligodendrocytes have only a few hours in which to generate new myelin sheaths in vivo. Dev. Cell 25, 599–609. [PubMed: 23806617]

Djannatian M, Timmler S, Arends M, Luckner M, Weil MT, Alexopoulos I, Snaidero N, Schmid B, Misgeld T, Möbius W, et al. (2019). Two adhesive systems cooperatively regulate axon ensheathment and myelin growth in the CNS. Nat. Commun. 10, 4794. [PubMed: 31641127]

Emery B, Agalliu D, Cahoy JD, Watkins TA, Dugas JC, Mulinyawe SB, Ibrahim A, Ligon KL, Rowitch DH, and Barres BA (2009). Myelin gene regulatory factor is a critical transcriptional regulator required for CNS myelination. Cell 138, 172–185. [PubMed: 19596243]

Emery B, and Dugas JC (2013). Purification of oligodendrocyte lineage cells from mouse cortices by immunopanning. Cold Spring Harb. Protoc. 2013, 854–868. [PubMed: 24003195]

Faul F, Erdfelder E, Buchner A, and Lang AG (2009). Statistical power analyses using G*Power 3.1: tests for correlation and regression analyses. Behav. Res. Methods 41, 1149–1160. [PubMed: 19897823]

Ferguson SM (2019). Neuronal lysosomes. Neurosci. Lett. 697, 1–9. [PubMed: 29626653]

Fields RD (2008). White matter in learning, cognition and psychiatric disorders. Trends Neurosci. 31, 361–370. [PubMed: 18538868]

Filimonenko M, Isakson P, Finley KD, Anderson M, Jeong H, Melia TJ, Bartlett BJ, Myers KM, Birkeland HCG, Lamark T, et al. (2010). The selective macroautophagic degradation of aggregated proteins requires the PI3P-binding protein Alfy. Mol. Cell 38, 265–279. [PubMed: 20417604]

Filley CM, and Fields RD (2016). White matter and cognition: making the connection. J. Neurophysiol. 116, 2093–2104. [PubMed: 27512019]

Fischer CA, and Morell P (1974). Turnover of proteins in myelin and myelin-like material of mouse brain. Brain Res. 74, 51–65. [PubMed: 4847603]

Fox LM, Kim K, Johnson CW, Chen S, Croce KR, Victor MB, Eenjes E, Bosco JR, Randolph LK, Dragatsis I, et al. (2020). Huntington's disease pathogenesis is modified in vivo by Alfy/Wdfy3 and selective macroautophagy. Neuron 105, 813–821.e6. [PubMed: 31899071]

Franklin RJM, and Ffrench-Constant C (2017). Regenerating CNS myelin - from mechanisms to experimental medicines. Nat. Rev. Neurosci. 18, 753–769. [PubMed: 29142295]

Frid K, Einstein O, Friedman-Levi Y, Binyamin O, Ben-Hur T, and Gabizon R (2015). Aggregation of MBP in chronic demyelination. Ann. Clin. Transl. Neurol. 2, 711–721. [PubMed: 26273684]

Fu MM, Nirschl JJ, and Holzbaur ELF (2014). LC3 binding to the scaffolding protein JIP1 regulates processive dynein-driven transport of autophagosomes. Dev. Cell 29, 577–590. [PubMed: 24914561]

Fujita N, Itoh T, Omori H, Fukuda M, Noda T, and Yoshimori T (2008). The Atg16L complex specifies the site of LC3 lipidation for membrane biogenesis in autophagy. Mol. Biol. Cell 19, 2092–2100. [PubMed: 18321988]

Fünfschilling U, Supplie LM, Mahad D, Boretius S, Saab AS, Edgar J, Brinkmann BG, Kassmann CM, Tzvetanova ID, Möbius W, et al. (2012). Glycolytic oligodendrocytes maintain myelin and long-term axonal integrity. Nature 485, 517–521. [PubMed: 22622581]

Goebbels S, Oltrogge JH, Kemper R, Heilmann I, Bormuth I, Wolfer S, Wichert SP, Möbius W, Liu X, Lappe-Siefke C, et al. (2010). Elevated phosphatidylinositol 3, 4, 5-trisphosphate in glia triggers cell-autonomous membrane wrapping and myelination. J. Neurosci. 30, 8953–8964. [PubMed: 20592216]

Gomez-Sanchez JA, Carty L, Iruarrizaga-Lejarreta M, Palomo-Irigoyen M, Varela-Rey M, Griffith M, Hantke J, Macias-Camara N, Azkargorta M, Aurrekoetxea I, et al. (2015). Schwann cell autophagy, myelinophagy, initiates myelin clearance from injured nerves. J. Cell Biol. 210, 153–168. [PubMed: 26150392]

Griffey CJ, and Yamamoto A (2022). Macroautophagy in CNS health and disease. Nat. Rev. Neurosci. 23, 411–427. [PubMed: 35505254]

Hagemeyer N, Goebbels S, Papiol S, Kästner A, Hofer S, Begemann M, Gerwig UC, Boretius S, Wieser GL, Ronnenberg A, et al. (2012). A myelin gene causative of a catatonia-depression syndrome upon aging. EMBO Mol. Med. 4, 528–539. [PubMed: 22473874]

Hara T, Nakamura K, Matsui M, Yamamoto A, Nakahara Y, Suzuki-Migishima R, Yokoyama M, Mishima K, Saito I, Okano H, and Mizushima N (2006). Suppression of basal autophagy in neural cells causes neurodegenerative disease in mice. Nature 441, 885–889. [PubMed: 16625204]

Hayashi-Nishino M, Fujita N, Noda T, Yamaguchi A, Yoshimori T, and Yamamoto A (2009). A subdomain of the endoplasmic reticulum forms a cradle for autophagosome formation. Nat. Cell Biol. 11, 1433–1437. [PubMed: 19898463]

Hill RA, Li AM, and Grutzendler J (2018). Lifelong cortical myelin plasticity and age-related degeneration in the live mammalian brain. Nat. Neurosci. 21, 683–695. [PubMed: 29556031]

Hollenbeck PJ (1993). Products of endocytosis and autophagy are retrieved from axons by regulated retrograde organelle transport. J. Cell Biol. 121, 305–315. [PubMed: 7682217]

Huang B, Wei W, Wang G, Gaertig MA, Feng Y, Wang W, Li XJ, and Li S (2015). Mutant huntingtin downregulates myelin regulatory factor-mediated myelin gene expression and affects mature oligodendrocytes. Neuron 85, 1212–1226. [PubMed: 25789755]

Ishii A, Furusho M, Dupree JL, and Bansal R (2016). Strength of ERK1/2 MAPK activation determines its effect on myelin and axonal integrity in the adult CNS. J. Neurosci. 36, 6471–6487. [PubMed: 27307235]

Jang SY, Shin YK, Park SY, Park JY, Lee HJ, Yoo YH, Kim JK, and Park HT (2016). Autophagic myelin destruction by Schwann cells during Wallerian degeneration and segmental demyelination. Glia 64, 730–742. [PubMed: 26712109]

Jeffries MA, Urbanek K, Torres L, Wendell SG, Rubio ME, and Fyffe-Maricich SL (2016). ERK1/2 activation in preexisting oligodendrocytes of adult mice drives new myelin synthesis and enhanced CNS function. J. Neurosci. 36, 9186–9200. [PubMed: 27581459]

Jeong H, Then F, Melia TJ Jr., Mazzulli JR, Cui L, Savas JN, Voisine C, Paganetti P, Tanese N, Hart AC, et al. (2009). Acetylation targets mutant huntingtin to autophagosomes for degradation. Cell 137, 60–72. [PubMed: 19345187]

Keirstead HS, and Blakemore WF (1997). Identification of post-mitotic oligodendrocytes incapable of remyelination within the demyelinated adult spinal cord. J. Neuropathol. Exp. Neurol. 56, 1191–1201. [PubMed: 9370229]

Komatsu M, Waguri S, Chiba T, Murata S, Iwata J.i., Tanida I, Ueno T, Koike M, Uchiyama Y, Kominami E, and Tanaka K (2006). Loss of autophagy in the central nervous system causes neurodegeneration in mice. Nature 441, 880–884. [PubMed: 16625205]

Komatsu M, Waguri S, Ueno T, Iwata J, Murata S, Tanida I, Ezaki J, Mizushima N, Ohsumi Y, Uchiyama Y, et al. (2005). Impairment of starvation-induced and constitutive autophagy in Atg7-deficient mice. J. Cell Biol. 169, 425–434. [PubMed: 15866887]

Kondiles BR, and Horner PJ (2017). Myelin plasticity, neural activity, and traumatic neural injury. Dev. Neurobiol. 78, 108–122. [PubMed: 28925069]

Lappe-Siefke C, Goebbels S, Gravel M, Nicksch E, Lee J, Braun PE, Griffiths IR, and Nave KA (2003). Disruption of Cnp1 uncouples oligodendroglial functions in axonal support and myelination. Nat. Genet. 33, 366–374. [PubMed: 12590258]

Lebrun-Julien F, Bachmann L, Norrmén C, Trötzmüller M, Köfeler H, Rüegg MA, Hall MN, and Suter U (2014). Balanced mTORC1 activity in oligodendrocytes is required for accurate CNS myelination. J. Neurosci. 34, 8432–8448. [PubMed: 24948799]

Lee Y, Morrison BM, Li Y, Lengacher S, Farah MH, Hoffman PN, Liu Y, Tsingalia A, Jin L, Zhang PW, et al. (2012). Oligodendroglia metabolically support axons and contribute to neurodegeneration. Nature 487, 443–448. [PubMed: 22801498]

Lynch-Day MA, and Klionsky DJ (2010). The Cvt pathway as a model for selective autophagy. FEBS Lett. 584, 1359–1366. [PubMed: 20146925]

Lyons DA, Naylor SG, Scholze A, and Talbot WS (2009). Kif1b is essential for mRNA localization in oligodendrocytes and development of myelinated axons. Nat. Genet. 41, 854–858. [PubMed: 19503091]

Maday S, and Holzbaur ELF (2012). Autophagosome assembly and cargo capture in the distal axon. Autophagy 8, 858–860. [PubMed: 22617438]

Maday S, and Holzbaur ELF (2014). Autophagosome biogenesis in primary neurons follows an ordered and spatially regulated pathway. Dev. Cell 30, 71–85. [PubMed: 25026034]

Maday S, Wallace KE, and Holzbaur ELF (2012). Autophagosomes initiate distally and mature during transport toward the cell soma in primary neurons. J. Cell Biol. 196, 407–417. [PubMed: 22331844]

Madisen L, Zwingman TA, Sunkin SM, Oh SW, Zariwala HA, Gu H, Ng LL, Palmiter RD, Hawrylycz MJ, Jones AR, et al. (2010). A robust and high-throughput Cre reporting and characterization system for the whole mouse brain. Nat. Neurosci. 13, 133–140. [PubMed: 20023653]

Makinodan M, Okuda-Yamamoto A, Ikawa D, Toritsuka M, Takeda T, Kimoto S, Tatsumi K, Okuda H, Nakamura Y, Wanaka A, and Kishimoto T (2013). Oligodendrocyte plasticity with an intact cell body in vitro. PLoS One 8, e66124. [PubMed: 23762472]

Mathys H, Davila-Velderrain J, Peng Z, Gao F, Mohammadi S, Young JZ, Menon M, He L, Abdurrob F, Jiang X, et al. (2019). Single-cell transcriptomic analysis of Alzheimer's disease. Nature 570, 332–337. [PubMed: 31042697]

Mizushima N, Yamamoto A, Matsui M, Yoshimori T, and Ohsumi Y (2004). In vivo analysis of autophagy in response to nutrient starvation using transgenic mice expressing a fluorescent autophagosome marker. Mol. Biol. Cell 15, 1101–1111. [PubMed: 14699058]

Pajevic S, Basser PJ, and Fields RD (2014). Role of myelin plasticity in oscillations and synchrony of neuronal activity. Neuroscience 276, 135–147. [PubMed: 24291730]

Pankiv S, Clausen TH, Lamark T, Brech A, Bruun JA, Outzen H, Øvervatn A, Bjørkøy G, and Johansen T (2007). p62/SQSTM1 binds directly to Atg8/LC3 to facilitate degradation of ubiquitinated protein aggregates by autophagy. J. Biol. Chem. 282, 24131–24145. [PubMed: 17580304]

Patzig J, Erwig MS, Tenzer S, Kusch K, Dibaj P, Möbius W, Goebbels S, Schaeren-Wiemers N, Nave KA, and Werner HB (2016). Septin/anillin filaments scaffold central nervous system myelin to accelerate nerve conduction. Elife 5, e17119. [PubMed: 27504968]

Revelo NH, Kamin D, Truckenbrodt S, Wong AB, Reuter-Jessen K, Reisinger E, Moser T, and Rizzoli SO (2014). A new probe for super-resolution imaging of membranes elucidates trafficking pathways. J. Cell Biol. 205, 591–606. [PubMed: 24862576]

Riccio P, Giovannelli S, Bobba A, Romito E, Fasano A, Bleve-Zacheo T, Favilla R, Quagliariello E, and Cavatorta P (1995). Specificity of zinc binding to myelin basic protein. Neurochem. Res. 20, 1107–1113. [PubMed: 8570016]

Rosen GD, and Harry JD (1990). Brain volume estimation from serial section measurements: a comparison of methodologies. J. Neurosci. Methods 35, 115–124. [PubMed: 2283883]

Safaiyan S, Kannaiyan N, Snaidero N, Brioschi S, Biber K, Yona S, Edinger AL, Jung S, Rossner MJ, and Simons M (2016). Age-related myelin degradation burdens the clearance function of microglia during aging. Nat. Neurosci. 19, 995–998. [PubMed: 27294511]

Saraswat Ohri S, Bankston AN, Mullins SA, Liu Y, Andres KR, Beare JE, Howard RM, Burke DA, Riegler AS, Smith AE, et al. (2018). Blocking autophagy in oligodendrocytes limits functional recovery after spinal cord injury. J. Neurosci. 38, 5900–5912. [PubMed: 29793971]

Savas JN, Toyama BH, Xu T, Yates JR 3rd, and Hetzer MW (2012). Extremely long-lived nuclear pore proteins in the rat brain. Science 335, 942. [PubMed: 22300851]

Schneider CA, Rasband WS, and Eliceiri KW (2012). NIH Image to ImageJ: 25 years of image analysis. Nat. Methods 9, 671–675. [PubMed: 22930834]

Simons M, Krämer EM, Thiele C, Stoffel W, and Trotter J (2000). Assembly of myelin by association of proteolipid protein with cholesterol- and galactosylceramide-rich membrane domains. J. Cell Biol. 151, 143–154. [PubMed: 11018060]

Simpson PB, Mehotra S, Lange GD, and Russell JT (1997). High density distribution of endoplasmic reticulum proteins and mitochondria at specialized Ca2+ release sites in oligodendrocyte processes. J. Biol. Chem. 272, 22654–22661. [PubMed: 9278423]

Smith RS, and Koles ZJ (1970). Myelinated nerve fibers: computed effect of myelin thickness on conduction velocity. Am. J. Physiol. 219, 1256–1258. [PubMed: 5473105]

Snaidero N, Möbius W, Czopka T, Hekking LHP, Mathisen C, Verkleij D, Goebbels S, Edgar J, Merkler D, Lyons DA, et al. (2014). Myelin membrane wrapping of CNS axons by PI(3, 4, 5)P3-dependent polarized growth at the inner tongue. Cell 156, 277–290. [PubMed: 24439382]

Snaidero N, Velte C, Myllykoski M, Raasakka A, Ignatev A, Werner HB, Erwig MS, Möbius W, Kursula P, Nave KA, and Simons M (2017). Antagonistic functions of MBP and CNP establish cytosolic channels in CNS myelin. Cell Rep. 18, 314–323. [PubMed: 28076777]

Strohm L, and Behrends C (2019). Glia-specific autophagy dysfunction in ALS. Semin. Cell Dev. Biol. 99, 172–182. [PubMed: 31132469]

Strømhaug PE, Berg TO, Fengsrud M, and Seglen PO (1998). Purification and characterization of autophagosomes from rat hepatocytes. Biochem. J. 335 (Pt 2), 217–224. [PubMed: 9761717]

Strømhaug PE, and Seglen PO (1993). Evidence for acidity of prelysosomal autophagic/endocytic vacuoles (amphisomes). Biochem. J. 291 (Pt 1), 115–121. [PubMed: 8471030]

Sun LO, Mulinyawe SB, Collins HY, Ibrahim A, Li Q, Simon DJ, Tessier-Lavigne M, and Barres BA (2018). Spatiotemporal control of CNS myelination by oligodendrocyte programmed cell death through the TFEB-PUMA Axis. Cell 175, 1811–1826.e21. [PubMed: 30503207]

Wake H, Lee PR, and Fields RD (2011). Control of local protein synthesis and initial events in myelination by action potentials. Science 333, 1647–1651. [PubMed: 21817014]

Wang F, Ren SY, Chen JF, Liu K, Li RX, Li ZF, Hu B, Niu JQ, Xiao L, Chan JR, and Mei F (2020). Myelin degeneration and diminished myelin renewal contribute to age-related deficits in memory. Nat. Neurosci. 23, 481–486. [PubMed: 32042174]

Watkins TA, Emery B, Mulinyawe S, and Barres BA (2008). Distinct stages of myelination regulated by γ-secretase and astrocytes in a rapidly myelinating CNS coculture system. Neuron 60, 555–569. [PubMed: 19038214]

Williamson JM, and Lyons DA (2018). Myelin dynamics throughout life: an ever-changing landscape? Front. Cell. Neurosci. 12, 424. [PubMed: 30510502]

Winterstein C, Trotter J, and Krämer-Albers EM (2008). Distinct endocytic recycling of myelin proteins promotes oligodendroglial membrane remodeling. J. Cell Sci. 121, 834–842. [PubMed: 18303048]

Yamamoto A, and Simonsen A (2012). Chapter 2: autophagosome maturation, endocytosis and neurodegenerative disease. In Autophagy of the Nervous System:Cellular Self-Digestion in Neurons and Neurological Diseases, Yue Z and Chu CT, eds. (World Science), pp. 33–50.

Yap CC, Digilio L, McMahon LP, Garcia ADR, and Winckler B (2018). Degradation of dendritic cargos requires Rab7-dependent transport to somatic lysosomes. J. Cell Biol. 217, 3141–3159. [PubMed: 29907658]

Ye X, Zhou XJ, and Zhang H (2018). Exploring the role of autophagy-related gene 5 (ATG5) yields important insights into autophagy in autoimmune/autoinflammatory diseases. Front. Immunol. 9, 2334. [PubMed: 30386331]

Yeung MSY, Zdunek S, Bergmann O, Bernard S, Salehpour M, Alkass K, Perl S, Tisdale J, Possnert G, Brundin L, et al. (2014). Dynamics of oligodendrocyte generation and myelination in the human brain. Cell 159, 766–774. [PubMed: 25417154]

Zuchero JB, Fu MM, Sloan SA, Ibrahim A, Olson A, Zaremba A, Dugas JC, Wienbar S, Caprariello AV, Kantor C, et al. (2015). CNS myelin wrapping is driven by actin disassembly. Dev. Cell 34, 152–167. [PubMed: 26166300]

Highlights

- Oligodendrocytes (OLGs) use macroautophagy to maintain myelin sheaths

- OLGs consolidate cytosolic cargo via Alfy-mediated selective autophagy

- Disruption of OLG macroautophagy produces cell-autonomous myelin abnormalities

- With age, OLG macroautophagy disruption leads to neurodegeneration and death
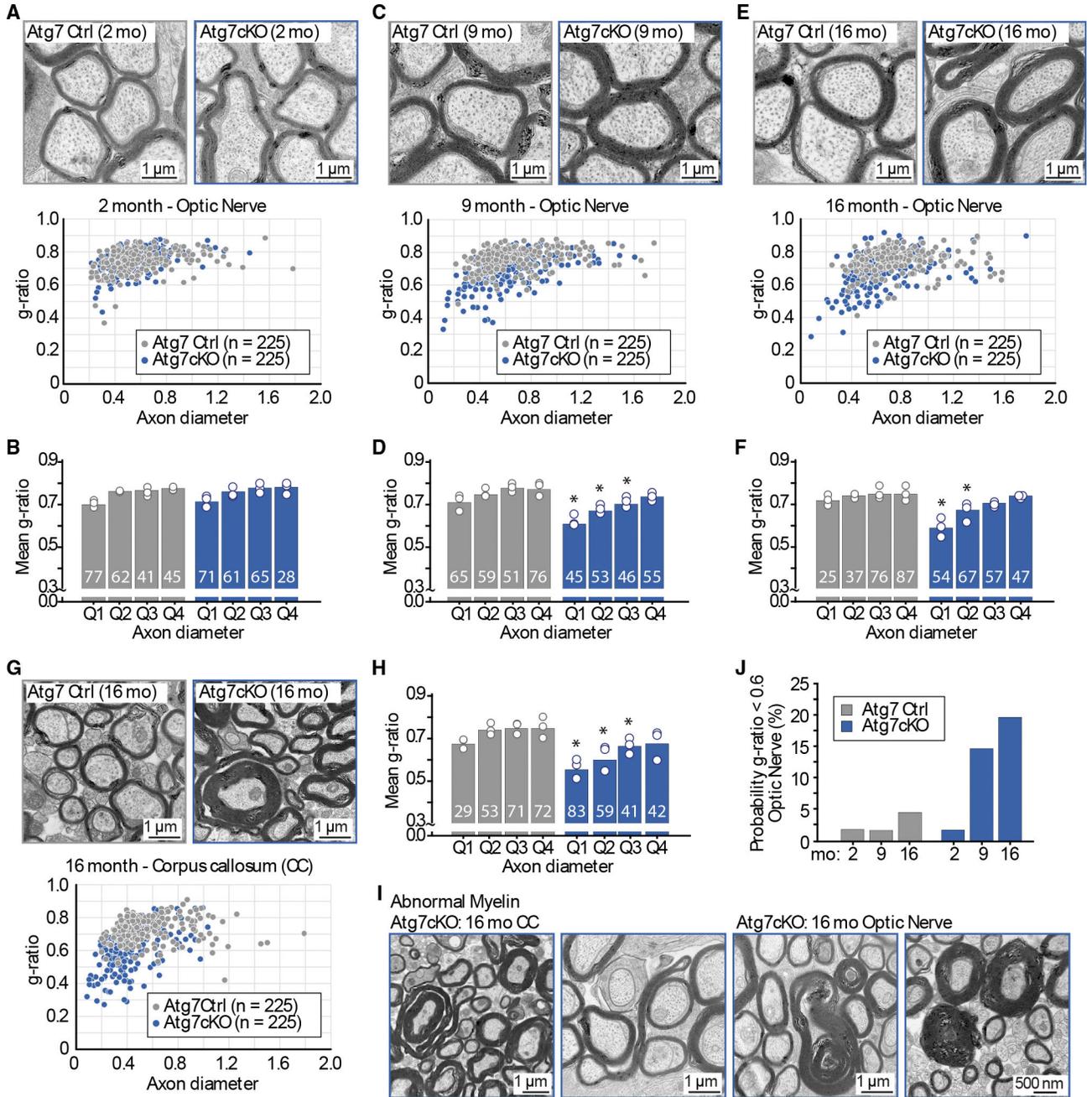
Figure 1. The inactivation of autophagy in OLGs results in an adult-onset accumulation of myelin, increased myelin sheath thickness, and abnormal myelin structures

(A–H) Ultrastructural images of myelin and g-ratio calculation from optic nerve at (A) 2, (C) 9, and (E) 16 months old and from (G) corpus callosum (CC) at 16 months old. n = 3 brains/genotype. (B, D, F, H) Mean g-ratios are plotted per quartile of axon diameter (μm). Bars represent average values across the 3 brains. The number of axons per quartile also shown. ANOVA reveals that in the optic nerve, there is no difference in mean g-ratios across quartiles at 2 months old (p = 0.5746; p = 0.9952; p = 0.3783; 0.5196). In contrast, g-ratios are significantly lower across the first 3 and 2 quartiles for 9 (p = 0.0473; p = 0.0179; p =

0.0256; p = 0.1951) and 16 months old (p = 0.0174; p = 0.0467; p = 0.072; p = 0.4738), respectively. CC also shows a similar difference (p = 0.0139; p = 0.0455; p = 0.0304; p = 0.2661). The axon diameters represented per quartile are as follows (upper value indicated): 2 (Q1 = 0.43, Q2 = 0.55, Q3 = 0.69, Q4 = 1.8), 9 (Q1 = 0.46, Q2 = 0.59, Q3 = 0.78, Q4 = 2.08), and 16 months old (Q1 = 0.50; Q2 = 0.63, Q3 = 0.80, Q4 = 1.77).

(I) Redundant myelin and myelin whorls in 16-month-old cKO CC (top) and optic nerve (bottom).

(J) Probability values of finding myelin g-ratio less than 0.6 of 225 axons examined at 2, 9, and 16 months old.
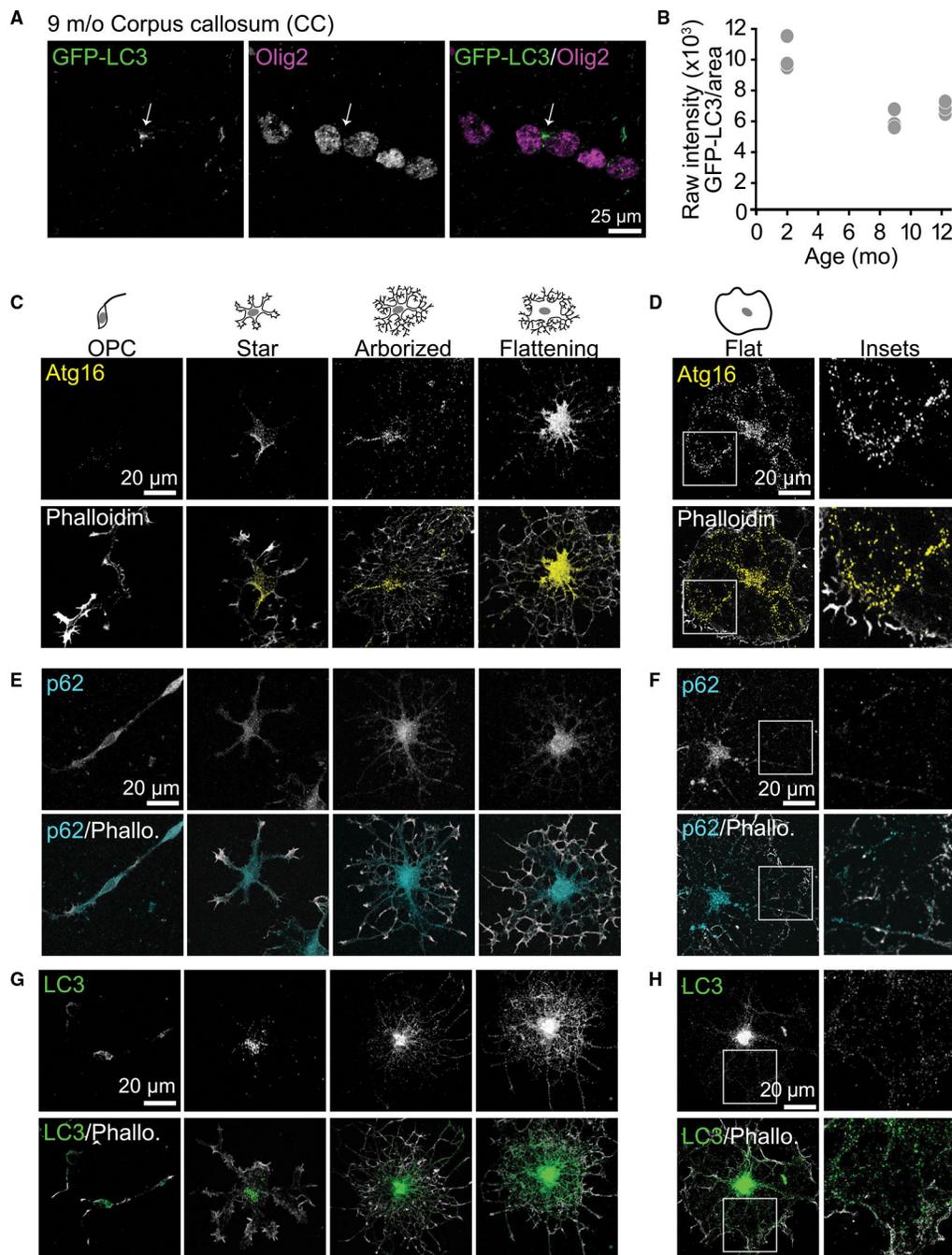
Figure 2. Basal autophagy in OLGs *in vivo* and in culture

(A and B) GFP-LC3$^+$ autophagosomes in OLGs in the adult brain under basal conditions. CC of GFP-LC3 transgenic mice was examined at 2, 9, and 12 months old. Acute treatment with chloroquine prevented autophagosome maturation.

(A) Representative image from 9-month-old CC.

(B) Quantification of raw integrated density value, sum of pixel intensity data (NIH ImageJ), of GFP-LC3 corrected for measured area (perinuclear of Olig2$^+$ cells) reveals that basal

autophagy is active in OLGs across time, with the highest activity at 2 months old. n = 3 brains/age.

(C–H) Immunofluorescence in different stages of OLG maturation. Staining against phalloidin (white) and (C and D) Atg16 (yellow), (E and F) p62 (cyan), and (G and H) LC3 (green) reveal a notable presence of all of these proteins throughout the cells during different stages of maturation. Mature OLGs with the boxed areas enlarged and shown at right highlight the presence of these proteins in the cytoplasmic channels of the myelin sheath. Representative images from n = 100 cells/3 litters.
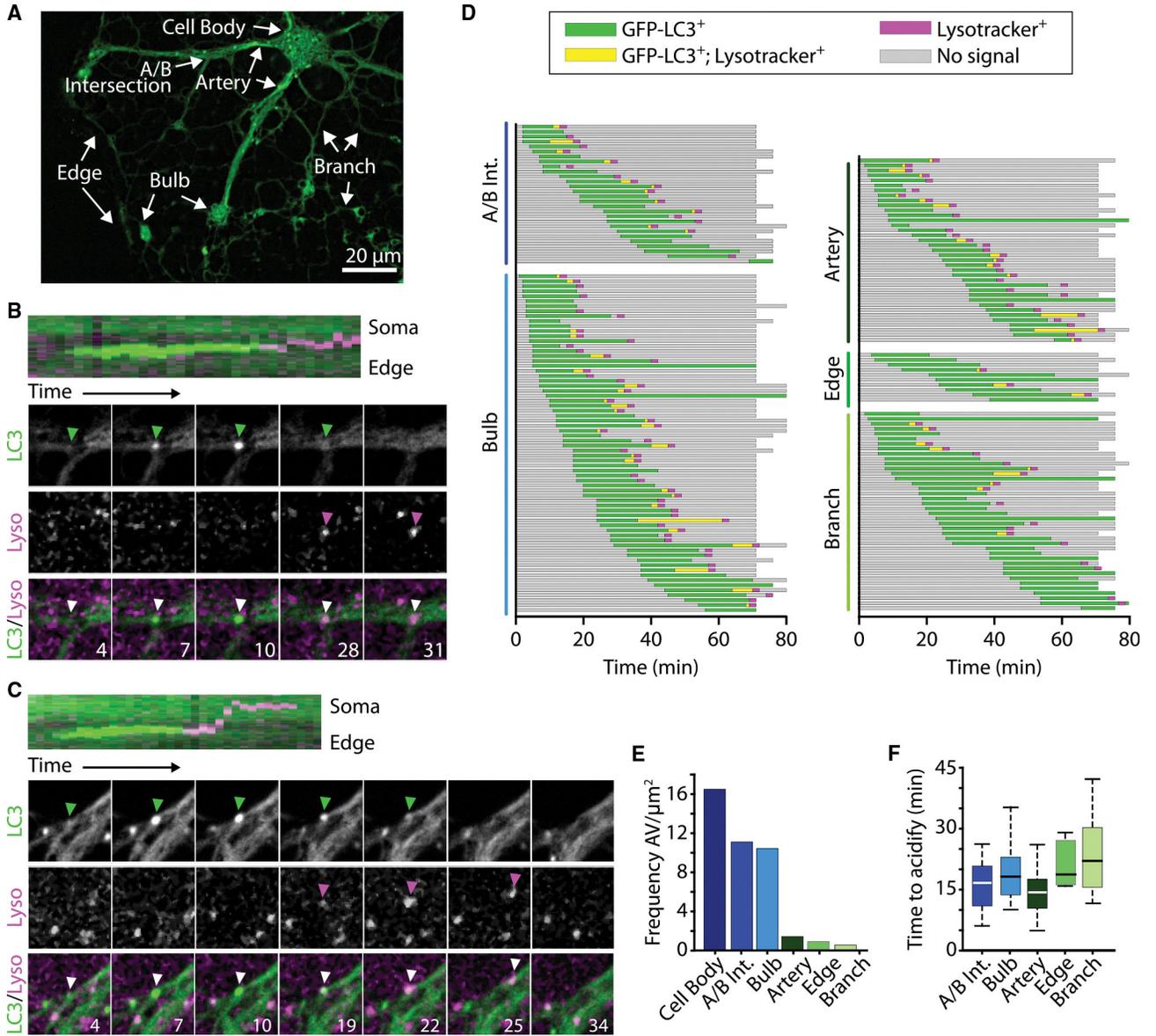
Figure 3. Autophagosome formation and maturation occurs throughout the mature OLs as revealed by live-cell imaging to capture selectively MBP

(A–C) GFP-LC3 in green, LysoTracker red in magenta, and overlay in white. Arrows indicate particle of interest. Time indicated in minutes.

(A) Regions of the mature OLG, taken from an individual cell. The cell is visually divided into discrete regions as indicated: cell body, artery, branch, artery/branch (A/B) intersection, bulb, and edge. Image taken from Video S2.

(B and C) Selected frames from Video S3. Additional particles are found in Video S3 and summarized in Figure S3.

(D–F) Summary of all movies analyzed.

(D) Each individual punctum analyzed across time. Green indicates the appearance of GFP-LC3 puncta, and magenta indicates positive signal for LysoTracker red. Co-localization represented in yellow. The formation of 185 GFP-LC3+ puncta analyzed across 6 movies

monitored throughout the cell, then analyzed for time through maturation. Structures that were only Lysotracker+ were not analyzed.

(E) Quantification of the frequency of autophagic vacuole (AV) appearance corrected for area.

(F) Time to acidify versus cell region. A/B Int., Artery-Branch intersection. Data from 143 cells/2 cultures.
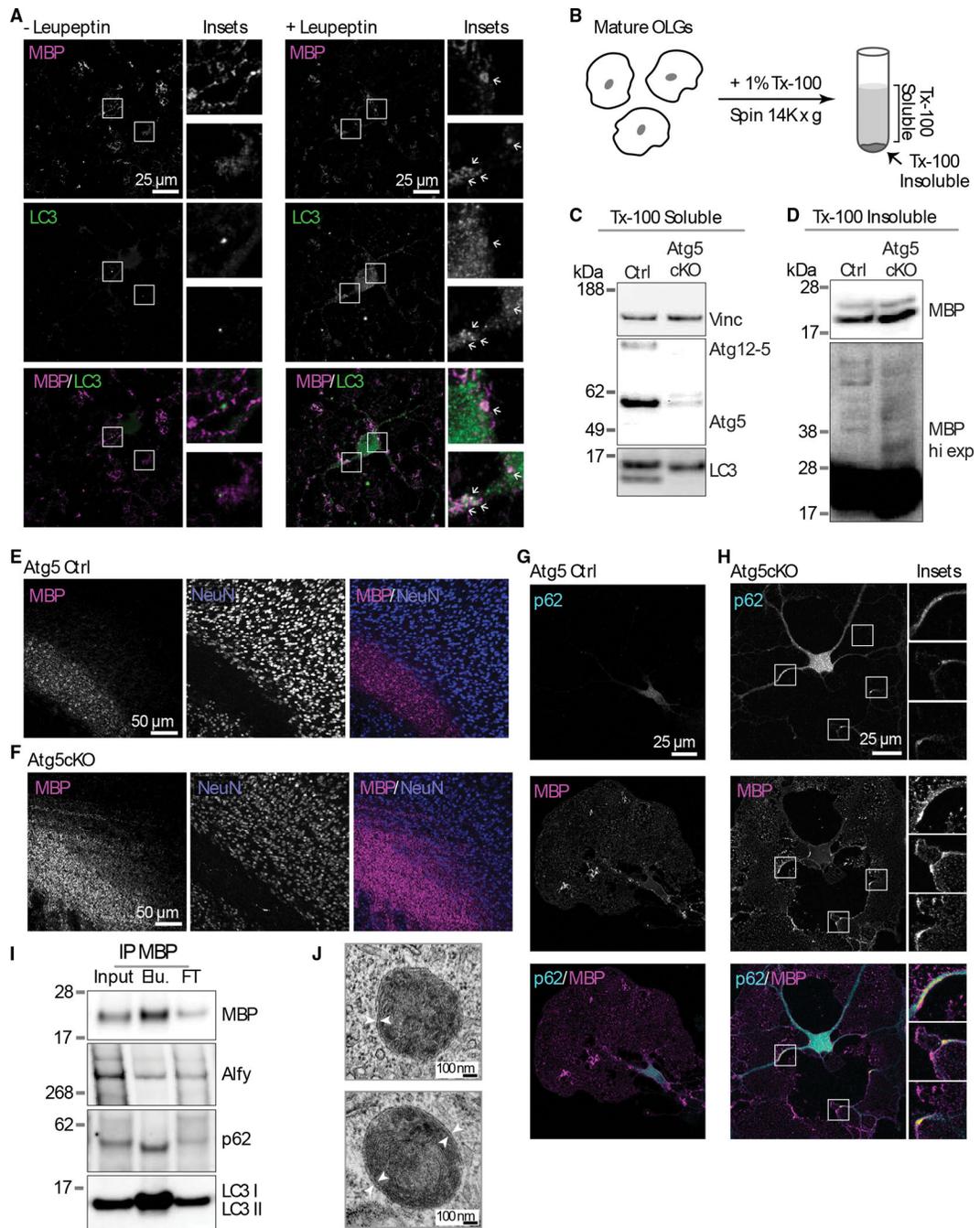
Figure 4. The oligodendrocyte protein MBP is degraded by selective autophagy

(A) Co-localization of MBP in autophagosomes. MBP (magenta) and endogenous LC3 (green) staining revealed upon lysosome inhibition. OLGs are treated with Leupeptin overnight to mildly impede lysosome function and promote autophagosome accumulation. Representative images from n = 90 cells/5 cultures.

(B–D) Increased presence of MBP in the detergent-insoluble fraction of Atg5cKO OLGs.

(B) Schematic representation.

(C and D) Western blot analysis of 1% Tx-100 (C) -soluble and (D) -insoluble Ctrl and cKO cell lysates. Probing the detergent insoluble pellet (resolubilized in 8 M urea) indicates greater accumulation of MBP in the absence of *Atg5*. Representative blots from n = 3 cultures/genotype.

(E and F) MBP (magenta) and NeuN (blue) in adult cortex from Atg5Ctrl and cKO mice.

(G and H) p62 and MBP in Atg5cKO OLGs. Accumulation of p62 (cyan) can be detected throughout the cKO cells. Co-staining for MBP (magenta) reveals that regions of p62 accumulation also have high MBP (shown in inset). Representative images from n = 60 cells/3 cultures/genotype.

(I) Co-immunoprecipitation (coIP) of endogenous Alfy, p62, and LC3 with MBP from wild-type brain tissue.

(J) Transmission electron microscopy analyses of mature OLGs in culture reveals the presence of large double-membrane structures filled with electron-dense material, but devoid of bulk cytosol, suggestive of aggregated cargoes captured via selective autophagy. Representative images from 20 cells/4 cultures.
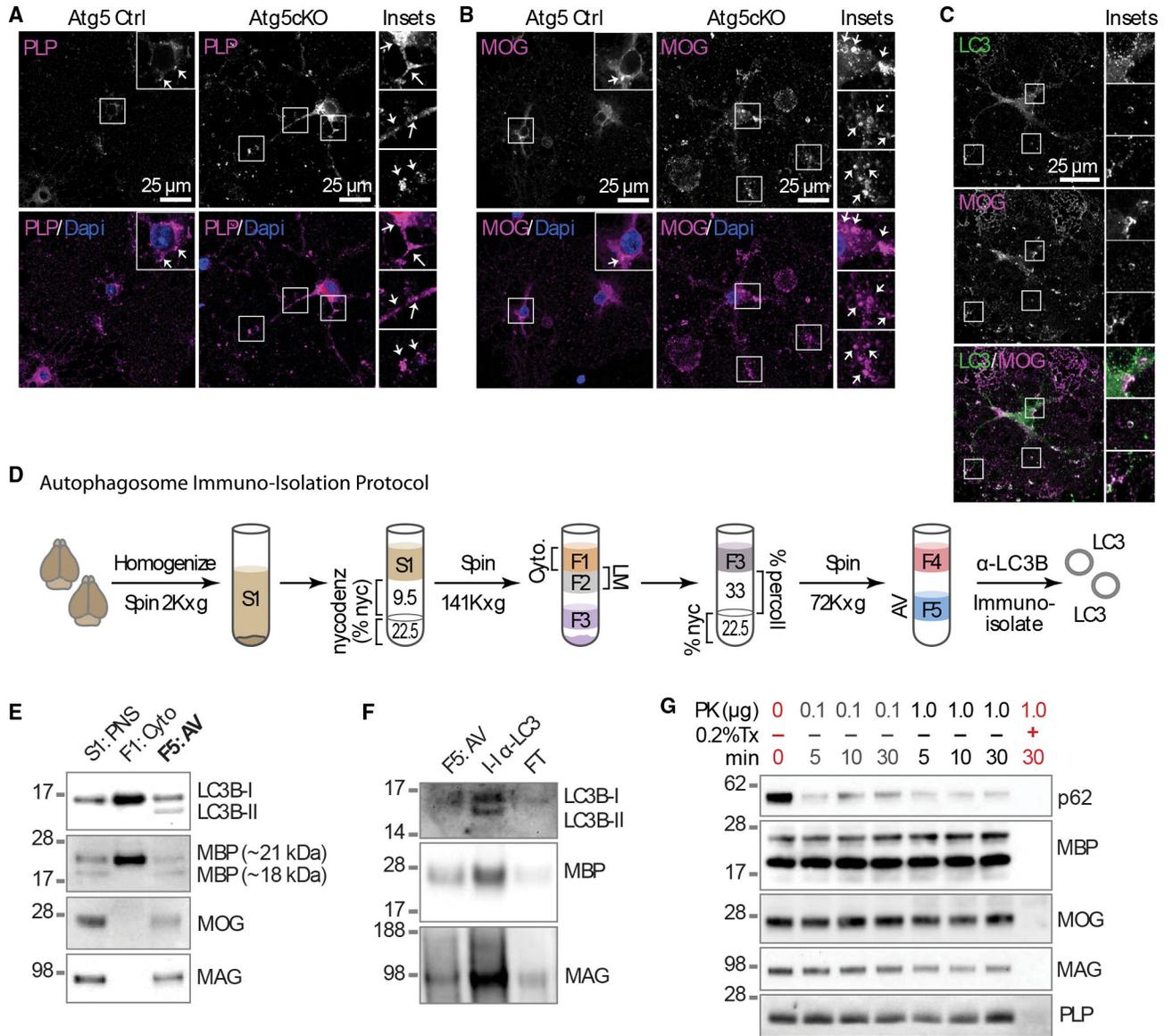
Figure 5. Integral membrane myelin proteins require macroautophagy for their degradation

(A and B) Endogenous (A) PLP and (B) MOG in Atg5Ctrl and cKO OLGs. Both proteins accumulate more frequently in Atg5cKO OLGs, as indicated by the number of punctate structures quantified per cell (PLP: Ctrl = 10.85 ± 6.15 versus cKO = 22.17 ± 8.42; two-tailed, Student's t test: p = 0.017; MOG: Ctrl = 9.11 ± 8.70 versus cKO = 46.43 ± 23.5; two-tailed, Student's t test: p < 0.001). Higher magnification shows areas of interest. n = 60 cells/3 cultures/genotype.

(C) MOG co-localizes with LC3$^+$ structures in wild-type (WT) OLGs.

(D–G) Fractionation of the adult brain reveals the presence of myelin associated proteins in AVs.

(D) AV isolation. Fractionation of the post nuclear supernatant (PNS, S1) across a step gradient of nycodenz (nyc) segregates S1 into 3 fractions (F1, F2, F3) and a pellet. F1 represents cytosol (Cyto), and F2 represents the light membrane (LM) fraction. F3 is further

fractionation across a Percoll gradient into F4 and F5. The densest fraction, F5, enriches for AVs.

(E) Immunoblotting reveals the presence of myelin proteins in the AV fractions.

(F) Immuno-isolation (I-I) of LC3$^+$ AVs leads to a further enrichment of myelin proteins.

(G) PK protection reveals that the myelin proteins are within AVs. 30 μg AVs are exposed to the noted amount of PK and incubated for the times shown. In the presence of detergent, and thereby upon membrane disruption, the proteins are susceptible to degradation by PK. Fractions from n = 5 brains/fractionation. Data representing n = 3 fractionations from 3- to 6-month-old mice.
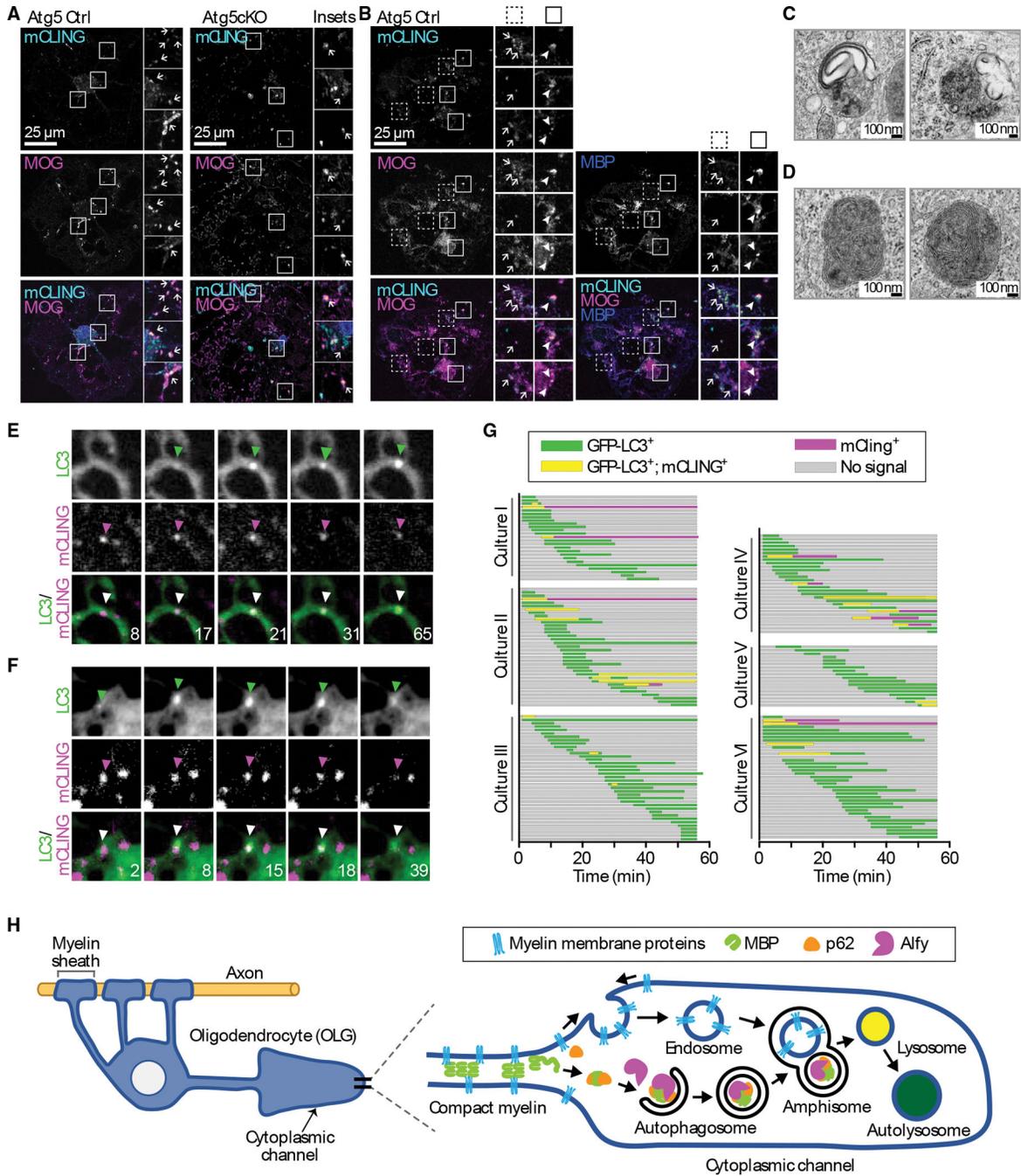
Figure 6. Myelin-associated integral membrane proteins such as MOG are internalized by endocytosis and then form an amphisome to be degraded

(A) Endocytosis of MOG as shown by overnight exposure to the surface membrane dye, mCLING. Atg5 Ctrl and cKO cultures reveal similar co-localization of MOG (magenta) and mCLING (cyan). n = 60 cells/3 cultures/genotype. Chi-square test reveals no significant difference between cKO and Ctrl cultures in the likelihood that MOG co-localizes to mCLING (chi-square statistic = 0.60594, p = 0.607).

(B) Co-staining of mCLING, MOG, and MBP. Triple staining shows that while MOG (magenta) and MBP (blue) can simultaneously co-localize with mCLING (cyan), MOG-

mCLING co-localization can also occur without MBP. Dashed-line boxes highlight MOG-mCLING localization events, whereas solid line boxes indicate sites of triple co-localization. n = 40 cells/2 cultures.

(C and D) EM analyses of mature OLGs in culture treated with Leupeptin overnight. Structures reminiscent of (C) amphisomes, double-membrane structures that appear fused with single-membrane vesicles filled with myelin-like membranes, are found throughout the cell, as well as (D) unilamellar autolysosomes. 20 cells/4 cultures.

(E–G) Live-cell imaging of GFP-LC3^{+} cells (green) treated with mCLING (magenta).

(E and F) Selected frames from Video S5 of individual puncta. Arrows indicate particle of interest. Time in minutes. A complete cell can be viewed in Video S4, and additional particles in Video S5, and summarized in Figure S6.

(G) Each individual puncta analyzed across time. Green indicates the appearance of GFP-LC3 puncta, and magenta indicates positive signal for mCLING. Co-localization represented in yellow. The formation of 187 GFP-LC3^{+} puncta analyzed across 6 movies monitored throughout the cell, then analyzed for mCLING fusion. Structures that were only mCLING[+] were not analyzed.

(H) Schematic model of the cell-autonomous turnover of myelin by macroautophagy. Aggregated MBP is taken up in a p62- and Alfy-dependent manner into an autophagosome via selective autophagy. These structures meet with endocytosed integral membrane myelin proteins to form an amphisome. The amphisome then fuses with a lysosome (yellow) to permit content degradation (dark green).
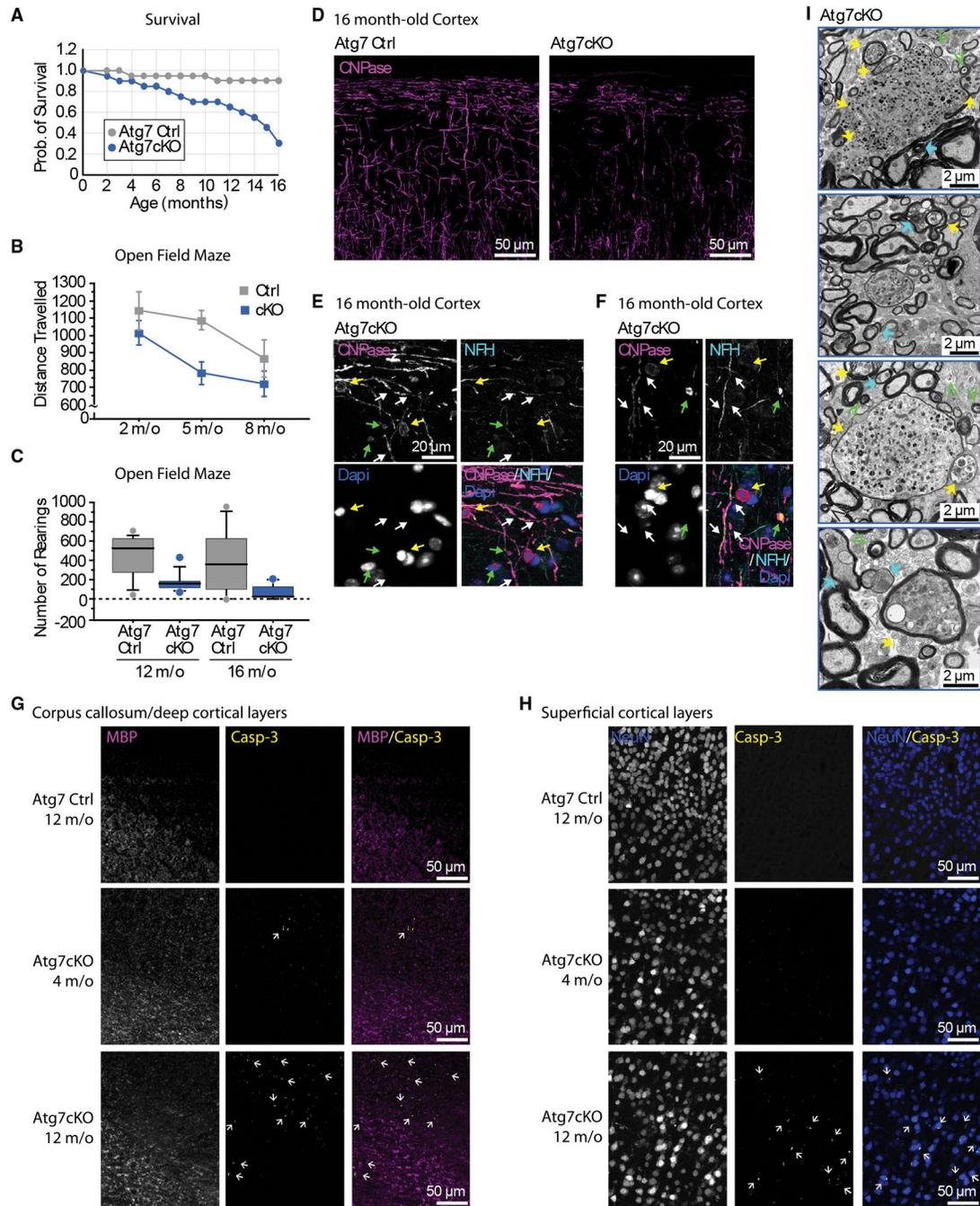
Figure 7. The inactivation of oligodendroglial autophagy results in behavioral deficits, neurodegeneration, and death

(A) Survival plot of Atg7cHet and cKO mice. n = 30 littermate pairs.

(B) Atg7cKO mice demonstrate locomotor deficits starting at 5 months old. The same cohort of mice (n = 15/genotype) are monitored for 5 min across time. Repeated measures ANOVA (RM-ANOVA) reveals a significant difference between genotype ($F_{(1,26)}$ = 5.212, p = 0.0308), with a significant decline starting at 5 months old in Atg7cKO (p = 0.0215) but not Ctrl (p = 0.5809). No difference was observed in rearing behavior at young ages (not shown).

(C) Rearing behavior monitored for 1 h at 12 or 16 months old. RM-ANOVA revealed a difference between genotype ($F_{(1, 29)}$ = 1.420; p = 0.0002), and Fisher's posthoc Least Significant Difference (LSD) reveals that it is different at 12 (p = 0.0041) and 16 months old (p = 0.0134).

(D–H) Loss of oligodendroglial macroautophagy leads to glial degeneration.

(D) Z projections of CNPase staining of the same volume of tissue from region matched areas of Atg7cHet and cKO mice at 16 months old (n = 3/genotype). No differences were observed at 9 or 12 months old (not shown, n = 3/genotype/age). The CNPase signal in cKO is noticeably decreased and patchier than in cHet.

(E and F) Higher magnification views of cKO tissue. CNPase (magenta) is co-stained with neurofilament heavy chain (NFH; cyan) and Dapi (blue). Ragged myelin sheaths (white arrow), accumulations within OL cell bodies (yellow arrow), and myelin blebs (green arrow) are observed in the cKO but not in the Ctrl (Figure S7A).

(G and H) Staining for activated caspase-3 (yellow) in the CC and cortex of 12-month-old Atg7Ctrl, 4-month-old Atg7cKO, and 12-month-old Atg7cKO mice. Staining reveals caspase-3[+] signal in 12-month-old Atg7cKO mice within the (G) MBP[+] (magenta) CC and (H) NeuN^{+} cortical neurons, with an occasional signal in the 4-month-old Atg7cKO and no signal in control brains. n = 3/genotype/age.

(I) EM micrographs of CC from 16-month-old Atg7cKO mice. Axonal spheroids (yellow arrows), aberrant OL structures (cyan arrows), and myelin debris (green v-arrowhead).

KEY RESOURCES TABLE

REAGENT or RESOURCE	SOURCE	IDENTIFIER
Antibodies		
Rat anti-MBP	Bio-Rad/Abd Serotec	MCA409S
Mouse anti-MBP	Covance	SM-199P
Mouse anti-APC [CC1]	abcam	ab16794
Rabbit anti-Olig2	Millipore	AB9610
Rabbit anti-NG2	Millipore	AB5320
Rabbit anti-PLP	abcam	Ab28486
Rabbit anti-MAG (D4G3)	Cell Signaling Technology	9043
Goat anti-MOG	abcam	Ab115597
Rabbit anti-BIII-tubulin	Covance	PRB-435P
Rabbit anti-Atg7 (D12B11)	Cell Signaling Technology	8558
Rabbit anti-Atg5	Cell Signaling Technology	12994
Rabbit anti-Vinculin	Invitrogen	700062
Rabbit anti-LC3A/B	abcam	Ab58610
Rabbit anti-LC3B	Abcam	Ab48394
Rabbit anti-Atg16	ProSci Inc.	4425
Guinea pig anti-p62	Progen	GP62C
Rabbit anti-Calnexin	Stressgen	SPA-860
Mouse anti-NeuN	Millipore	MAB377
Rabbit anti-Cre Recombinase (D7L7L)	Cell Signaling Technology	15036
Rabbit anti-cleaved Caspase-3 (Asp175)	Cell Signaling Technology	9661
pM_CNPase	Biolegend	836404
pC_NFH-H	Encor	CPCA-NF-H
pRb_NeuN	Abcam	ab177487
O4	R&D Systems	MAB1326
Chemicals, peptides, and recombinant proteins		
Transferrin	Sigma	T1147
Bovine serum albumin	Sigma	A4161
Putrescine	Sigma	P5780
Progesterone	Sigma	P8783
Sodium selenite	Sigma	S5261
N-acetyl-L-cysteine	Sigma	A8199
D-biotin	Sigma	B4639
Forskolin	Sigma	F6886
Insulin	Sigma	I6634
Glutamine	Invitrogen	25030081
Sodium pyruvate	Invitrogen	11360070
B27	Invitrogen	17504044

REAGENT or RESOURCE	SOURCE	IDENTIFIER
Penicillin-streptomycin	Invitrogen	15140122
Trace Elements B	Corning/Cellgro	MT99175CI
LIF	Sigma	ESG1107
PDGF-AA	PeproTech	100-13A
NT-3	PeproTech	450-03
Triiodothyronine	Sigma	T6397
TRIzol	ThermoFisher	450-03
Hoechst	Invitrogen	H3570
NeuroTrace	ThermoFisher	N21479
Halt protease inhibitor cocktail	ThermoFisher	78430
PMSF	Sigma	P7626
BSL1	Vector Laboratories	L1100
Leupeptin	Sigma	L5793
mCLING	Synaptic Systems	710 006AT1
LysoTracker red DND-99	Invitrogen	L7528
Alexa Fluor™ 594 C5 Maleimide	ThermoFisher	A10256
Critical commercial assays		
AMV Reverse Transcription System	Promega	M5101
Papain dissociation system	Worthington	PDS
mCLING labeling kit	Synaptic Systems	710-MCK
DC protein assay	Bio-Rad	5000111
Experimental models: Organisms/strains		
Mouse: CNP-Cre (Cnp^tm1(cre)Kan)	Klaus-Armin Nave, Max Planck Institute, Germany	Lappe-Siefke et al., 2003
Mouse: Atg7-floxed	Masaaki Komatsu, Juntendo University, Japan	Komatsu et al., 2005
Mouse: Atg5-floxed	Noboru Mizushima, University of Tokyo, Japan	Hara et al., 2006
Mouse: GFP-LC3	Noboru Mizushima, University of Tokyo, Japan	Mizushima et al., 2004
Mouse: TdTomato/Ai9 (B6.Cg-Gt(ROSA) 26Sor^tm9(CAG-tdTomato)Hze/J)	Jackson Laboratory	RRID: IMSR_JAX:007,909 (Madisen et al., 2010)
Oligonucleotides		
Atg7 flox PCR 1: CAT CTT GTA GCA CCT GCT GAC CTG G	RIKEN BioResource Center	Protocol: 02760
Atg7 flox PCR 2: CCA CTG GCC CAT CAG TGA GCA TG	RIKEN BioResource Center	Protocol: 02760
Atg7 flox PCR 3: GCG GAT CCT CGT ATA ATG TAT GCT AT	RIKEN BioResource Center	Protocol: 02760
Atg5 flox PCR 1: GAA TAT GAA GGC ACA CCC CTG AAA TG	Hara et al., 2006	N/A
Atg5 flox PCR 2: GTA CTG CAT AAT GGT TTA ACT CTT GC	Hara et al., 2006	N/A
Atg5 flox PCR 3: ACA ACG TCG AGC ACA GCT GCG CAA GG	Hara et al., 2006	N/A
Atg5 flox PCR 4: CAG GGA ATG GTG TCT CCC AC	Hara et al., 2006	N/A
CNP-Cre PCR E3 sense: GCC TTC AAA CTG TCC ATC TC	Lappe-Siefke et al., 2003	N/A

REAGENT or RESOURCE	SOURCE	IDENTIFIER
CNP-Cre PCR E3 antisense: CCC AGC CCT TTT ATT ACC AC	Lappe-Siefke et al., 2003	N/A
CNP-Cre PCR Puro3: CAT AGC CTG AAG AAC GAG A	Lappe-Siefke et al., 2003	N/A
GFP-LC3 PCR 1: ATA ACT TGC TGG CCT TTC CAC T	RIKEN BioResource Center	Protocol: 00,806
GFP-LC3 PCR 2: CGG GCC ATT TAC CGT AAG TTA T	RIKEN BioResource Center	Protocol: 00806
GFP-LC3 PCR 3: GCA GCT CAT TGC TGT TCC TCA A	RIKEN BioResource Center	Protocol: 00806
tdTomato PCR WT F: AAG GGA GCT GCA GTG GAG TA	Jackson	Protocol: 29436
tdTomato PCR WT R: CCG AAA ATC TGT GGG AAG TC	Jackson	Protocol: 29436
tdTomato PCR TG F: CTG TTC CTG TAC GGC ATG G	Jackson	Protocol: 29436
tdTomato PCR TG R: GGC ATT AAA GCA GCG TAT CC	Jackson	Protocol: 29436
beta-actin RT-PCR 1: AGC CTT CCT TCT TGG GTA TG	NCBI	N/A
beta-actin RT-PCR 2: GGT CTT TAC GGA TGT CAA CG	NCBI	N/A
MBP RT-PCR 1: GGC CTC AGA GGA CAG TGA TG	Lebrun-Julien et al., 2014	N/A
MBP RT-PCR 2: TCT GCT GTG TGC TTG GAG TC	Lebrun-Julien et al., 2014	N/A
MOG RT-PCR 1: TGC ACC GAA GAC TGG CAG GAC	Lebrun-Julien et al., 2014	N/A
MOG RT-PCR 2: AAG GAC CTG CTG GGC TCT CCT	Lebrun-Julien et al., 2014	N/A
PLP RT-PCR 1: GTT CCA GAG GCC AAC ATC AAG CTC	Lebrun-Julien et al., 2014	N/A
PLP RT-PCR 2: AGC CAT ACA ACA GTC AGG GCA TAG	Lebrun-Julien et al., 2014	N/A
Software and algorithms		
NIH ImageJ	Schneider et al., 2012	N/A
StatView	SAS Institute Inc.	N/A
MATLAB	Mathworks	N/A
Open field activity	Med Associates Inc.	MED-OFAS-MSU
Photoshop CS5, llustrator CS5	Adobe	N/A
Other		
Protein A/G MicroBeads	Miltenyi Biotec	130-071-001/130-071-101
μ columns	Miltenyi Biotec	130-042-701